

# MRS: a noninvasive window into cardiac metabolism

Citation for published version (APA):

van Ewijk, P. A., Schrauwen-Hinderling, V. B., Bekkers, S. C., Glatz, J. F., Wildberger, J. E., & Kooi, M. E. (2015). MRS: a noninvasive window into cardiac metabolism. *NMR in Biomedicine*, 28(7), 747-766. <https://doi.org/10.1002/nbm.3320>

**Document status and date:**

Published: 01/01/2015

**DOI:**

[10.1002/nbm.3320](https://doi.org/10.1002/nbm.3320)

**Document Version:**

Publisher's PDF, also known as Version of record

**Document license:**

Taverne

**Please check the document version of this publication:**

- A submitted manuscript is the version of the article upon submission and before peer-review. There can be important differences between the submitted version and the official published version of record. People interested in the research are advised to contact the author for the final version of the publication, or visit the DOI to the publisher's website.
- The final author version and the galley proof are versions of the publication after peer review.
- The final published version features the final layout of the paper including the volume, issue and page numbers.

[Link to publication](#)

**General rights**

Copyright and moral rights for the publications made accessible in the public portal are retained by the authors and/or other copyright owners and it is a condition of accessing publications that users recognise and abide by the legal requirements associated with these rights.

- Users may download and print one copy of any publication from the public portal for the purpose of private study or research.
- You may not further distribute the material or use it for any profit-making activity or commercial gain
- You may freely distribute the URL identifying the publication in the public portal.

If the publication is distributed under the terms of Article 25fa of the Dutch Copyright Act, indicated by the "Taverne" license above, please follow below link for the End User Agreement:

[www.umlib.nl/taverne-license](http://www.umlib.nl/taverne-license)

**Take down policy**

If you believe that this document breaches copyright please contact us at:

[repository@maastrichtuniversity.nl](mailto:repository@maastrichtuniversity.nl)

providing details and we will investigate your claim.

# MRS: a noninvasive window into cardiac metabolism

Petronella A. van Ewijk<sup>a,b,c</sup>, Vera B. Schrauwen-Hinderling<sup>a,b,c</sup>, Sebastiaan C. A. M. Bekkers<sup>d</sup>, Jan F. C. Glatz<sup>e,f</sup>, Joachim E. Wildberger<sup>b</sup> and M. Eline Kooi<sup>b,c,f,\*</sup>

A well-functioning heart requires a constant supply of a balanced mixture of nutrients to be used for the production of adequate amounts of adenosine triphosphate, which is the main energy source for most cellular functions. Defects in cardiac energy metabolism are linked to several myocardial disorders. MRS can be used to study *in vivo* changes in cardiac metabolism noninvasively. MR techniques allow repeated measurements, so that disease progression and the response to treatment or to a lifestyle intervention can be monitored. It has also been shown that MRS can predict clinical heart failure and death. This article focuses on *in vivo* MRS to assess cardiac metabolism in humans and experimental animals, as experimental animals are often used to investigate the mechanisms underlying the development of metabolic diseases. Various MR techniques, such as cardiac <sup>31</sup>P-MRS, <sup>1</sup>H-MRS, hyperpolarized <sup>13</sup>C-MRS and Dixon MRI, are described. A short overview of current and emerging applications is given. Cardiac MRS is a promising technique for the investigation of the relationship between cardiac metabolism and cardiac disease. However, further optimization of scan time and signal-to-noise ratio is required before broad clinical application. In this respect, the ongoing development of advanced shimming algorithms, radiofrequency pulses, pulse sequences, (multichannel) detection coils, the use of hyperpolarized nuclei and scanning at higher magnetic field strengths offer future perspective for clinical applications of MRS. Copyright © 2015 John Wiley & Sons, Ltd.

**Keywords:** cardiac metabolism; MRS; Dixon MRI; animal; human

## INTRODUCTION

### Cardiac energy metabolism

The heart is an energy-demanding organ requiring a continuous supply of nutrients and oxygen. A schematic overview of cardiac energy metabolism is presented in Fig. 1. To meet this energy demand, large amounts of long-chain fatty acids (LCFAs) and

carbohydrates are metabolized to produce adenosine triphosphate (ATP). In the newborn heart, carbohydrates are the major energy-providing substrates (1), whereas the healthy adult heart obtains approximately 70% of its energy from LCFA oxidation and the remainder mostly from carbohydrate oxidation.

The uptake of LCFA into cardiomyocytes is facilitated by membrane proteins [fatty acid transport proteins (FATPs): CD36,

\* Correspondence to: M. Eline Kooi, Department of Radiology, Maastricht University Medical Center, PO Box 5800, 6202 AZ Maastricht, the Netherlands. E-mail: eline.kooi@mumc.nl

a P. A. Ewijk, V. B. Schrauwen-Hinderling  
Maastricht University Medical Center, Human Biology, Maastricht, the Netherlands

b P. A. Ewijk, V. B. Schrauwen-Hinderling, J. E. Wildberger, M. E. Kooi  
Maastricht University Medical Center, Radiology, Maastricht, the Netherlands

c P. A. Ewijk, V. B. Schrauwen-Hinderling, M. E. Kooi  
Maastricht University Medical Center, NUTRIM - School for Nutrition, Toxicology and Metabolism, Maastricht, the Netherlands

d S. C. A. M. Bekkers  
Maastricht University Medical Center, Cardiology, Maastricht, the Netherlands

e J. F. C. Glatz  
Maastricht University Medical Center, Molecular Genetics, Maastricht, the Netherlands

f J. F. C. Glatz, M. E. Kooi  
Maastricht University Medical Center, CARIM - Cardiovascular Research Institute Maastricht, Maastricht, the Netherlands

**Abbreviations used:** 1D, 2D, 3D, one-, two-, three-dimensional; 2,3-DPG, 2,3-diphosphoglycerate; AAT, alanine transaminase; ADP, adenosine diphosphate; ATP, adenosine triphosphate; CHESS, chemical shift-selective water suppression; CK, creatine kinase; CNR, contrast-to-noise ratio; CoA, coenzyme A; Cr, creatine; CSI, chemical shift imaging; DNP, dynamic nuclear polarization; ECG, electrocardiogram; EPSI, echo-planar spectroscopic imaging; ETC, electron transport chain; FADH<sub>2</sub>, reduced flavin adenine dinucleotide; FAST, four-angle saturation transfer; FATP, fatty acid transport protein; FID, free induction decay; GTP, guanosine triphosphate; IDEAL, iterative decomposition of water and fat with echo asymmetry and least-squares estimation; ISIS, image-selected *in vivo* spectroscopy; LCAD, long-chain acyl-CoA dehydrogenase; LCFA, long-chain fatty acid; LDH, lactate dehydrogenase; mDixon, modified Dixon technique; MTS, magnetization transfer spectroscopy; NADH, reduced nicotinamide adenine dinucleotide; NOE, nuclear Overhauser enhancement; O-DAM, ongoing dual-angle method; PCr, phosphocreatine; PDC, pyruvate dehydrogenase complex; PDH, pyruvate dehydrogenase; PDK, pyruvate dehydrogenase kinase; Pi, inorganic phosphate; ppm, parts per million; PPARα, peroxisome proliferator-activated receptor alpha; PRESS, point-resolved spectroscopy; RF, radiofrequency; SAR, specific absorption rate; SDAM, saturated double-angle method; SLOOP, spatial localization with optimal point spread function; SNR, signal-to-noise ratio; STEAM, stimulated echo acquisition mode; T2DM, type 2 diabetes mellitus; TCA, tricarboxylic acid; TG, triglyceride; VARPRO, variable projection; VLCAD, very-long-chain acyl-CoA dehydrogenase; VOI, volume of interest.

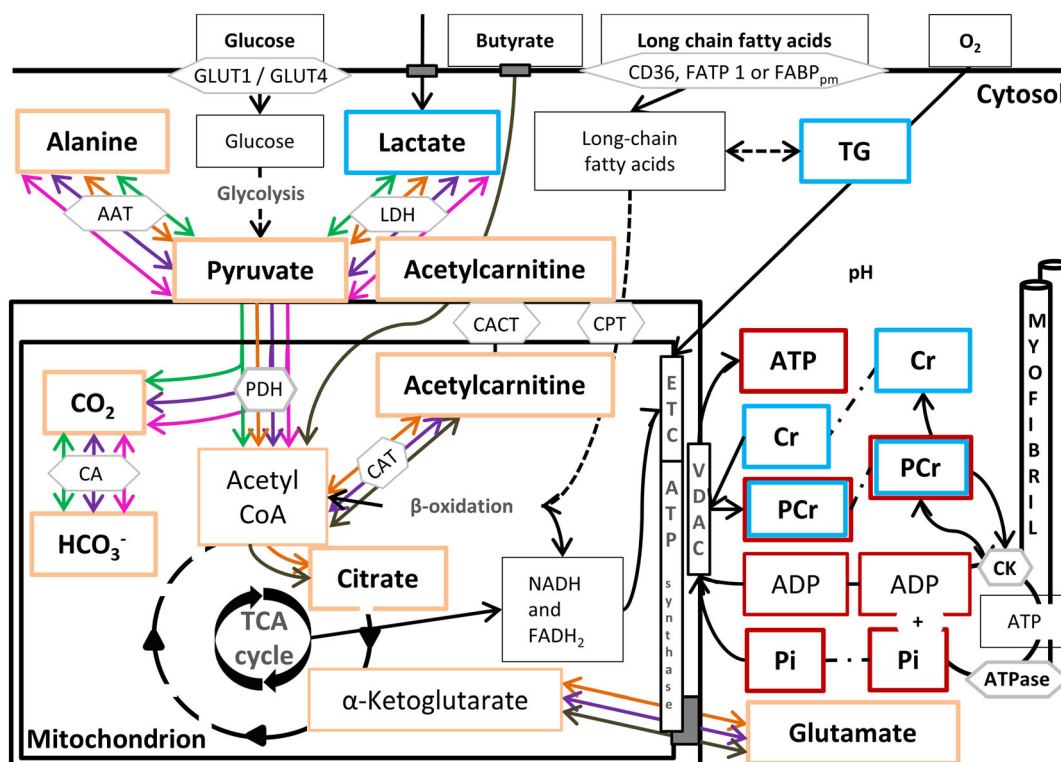


**Figure 1.** Metabolites detected in cardiomyocytes using MR techniques.  $^1\text{H}$ -MRS can be used for the detection of TGs, (total) creatine and lactate, which are indicated by the blue boxes. In addition, Dixon MRI can be used to detect myocardial TG content.  $^{31}\text{P}$ -MRS can be used for the detection of ATP, PCr, Pi and ADP, which are indicated by the red boxes. In addition,  $^{31}\text{P}$ -MTS can be used to measure the flux through the CK reaction and the ATP synthesis flux, as well as the intracellular pH, by measuring the chemical shift displacement between PCr and Pi. Using hyperpolarized  $^{13}\text{C}$ -MRS, several metabolites and fluxes can be determined, dependent on the hyperpolarized substrate used. Green arrows indicate the detectable metabolites from  $[1-^{13}\text{C}]$ pyruvate, orange arrows indicate the detectable metabolites from  $[2-^{13}\text{C}]$ pyruvate, purple arrows indicate the detectable metabolites from  $[1,2-^{13}\text{C}]$ pyruvate, pink arrows indicate the detectable metabolites from  $[1-^{13}\text{C}]$ lactate and some detectable metabolites from  $[1-^{13}\text{C}]$ butyrate are indicated with brown arrows. AAT, alanine transaminase; ADP, adenosine diphosphate; ATP, adenosine triphosphate; CA, carbonic anhydrase; CACT, carnitine-acylcarnitine translocase; CAT, carnitine acetyltransferase; CK, creatine kinase enzyme; CPT, carnitine palmitoyltransferase; Cr, creatine; ETC, electron transport chain;  $\text{FADH}_2$ , reduced flavin adenine dinucleotide; GLUT1/GLUT4, glucose transporters; LDH, lactate dehydrogenase; NADH, reduced nicotinamide adenine dinucleotide; PCr, phosphocreatine; PDH, pyruvate dehydrogenase; TCA, tricarboxylic acid; TG, triglyceride; VDAC, voltage-dependent anion channel.

FATP1 and FATP<sub>pm</sub>]; thereafter, LCFAs are converted into fatty acyl-coenzyme A (CoA) to be stored as triglycerides (TGs) or to be degraded into acetyl-CoA, via  $\beta$ -oxidation, thereby generating reduced nicotinamide adenine dinucleotide (NADH) and reduced flavin adenine dinucleotide (FADH<sub>2</sub>). More NADH and guanosine triphosphate (GTP) (which is energetically equivalent to ATP) are generated in the tricarboxylic acid (TCA) cycle.

Carbohydrates enter the cardiomyocyte via glucose transporters (GLUT1 and GLUT4). Glucose is converted (via glycolysis) into pyruvate, which is also produced from lactate and from alanine. Pyruvate passes the double membrane of the mitochondrion and is converted into acetyl-CoA via the pyruvate dehydrogenase (PDH) complex. Acetyl-CoA enters the TCA cycle or can be converted to acetylcarnitine. During glycolysis, NADH and ATP are also produced.

NADH is used for the generation of ATP through energy transfer via the electron transport chain (ETC) to ATP synthase. The high-energy phosphate bond from ATP can be transferred to creatine (Cr) to form phosphocreatine (PCr) and adenosine diphosphate (ADP). This reaction is catalyzed by the enzyme creatine kinase (CK). PCr diffuses through the cytosol to sites of utilization (e.g. myofibrils), where the high-energy phosphate from PCr is transferred to ADP to form ATP and Cr again.

In addition to LCFAs and carbohydrates, the heart also uses lactate and ketone bodies as an energy source (2).

Under pathophysiological conditions, substrate preference and TCA cycle activity can change, which may interfere with cardiac function (3).

## Metabolism in cardiac disease

Various cardiac diseases, ischemic as well as nonischemic, but also obesity, diabetes and aging, have been associated with an altered cardiac energy metabolism (4,5). In ischemic heart disease, substrate metabolism changes in relation to the severity of ischemia. In severe ischemia (>70% reduction in flow), the heart produces lactate that accumulates, whereas glycogen and high-energy phosphate levels decline, followed by contractile dysfunction and, ultimately, cell death. Mild to moderate ischemia (20–60% reduction in flow) is characterized by a transient lactate production, decreased high-energy phosphate levels and contractile dysfunction (4). Nonischemic cardiomyopathies are characterized by an increased reliance on glucose, and decreased LCFA uptake and oxidation (5). Obesity and diabetes are associated with an increased risk of heart failure (6,7). Here, the increased supply and uptake of LCFA (8–10) may lead to lipid

accumulation, which has been associated with metabolic changes, termed 'lipotoxicity' (11,12).

### MRS: a noninvasive window into cardiac metabolism

Because of its high temporal and spatial resolution, multiplanar imaging capabilities and high soft tissue contrast, cardiac MRI has become an established imaging technique for the study of myocardial structure, function, perfusion and focal fibrosis (13,14). Conventional cardiac MRI does not provide information on cardiac metabolism. However, cardiac MRS enables the study of *in vivo* changes in cardiac metabolism (15). In this way, MRS provides an insight into the changes in cardiac metabolism associated with cardiac disease. Because it allows repeated measurements, changes in cardiac metabolism during the (early) development of disease or in response to treatment or lifestyle intervention can be assessed. Furthermore, it has been shown that MRS can predict clinical heart failure and death in certain patient groups (16,17).

Cardiac MRS can be applied in humans as well as in animal models of disease. Animal models are often used to study the underlying metabolic pathways of cardiac disease. In addition, the use of animals enables a comparison of *in vivo* cardiac MRS with *in vitro* measurements to enable the validation of new techniques. Although small animals (especially mice) are often used to study metabolic pathways, investigations in larger animals (such as dogs and pigs) are valuable to validate measurements that can also be used in a clinical setting.

Several products from metabolic pathways can be detected using MRS, as depicted in Fig. 1. Metabolites derived from lipid and carbohydrate metabolism can be detected using  $^1\text{H}$ -MRS (18) and hyperpolarized  $^{13}\text{C}$ -MRS (19). Dixon MRI can be used to quantify cardiac lipid content (20). High-energy phosphates can be detected using  $^{31}\text{P}$ -MRS (21). Importantly, cardiac MRS can be performed in the same session as cardiac MRI.

### Outline

This article focuses on the methods that can be employed to assess cardiac metabolism *in vivo* using MRS and Dixon MRI in humans and experimental animals, with a main focus on  $^{31}\text{P}$ -MRS,  $^1\text{H}$ -MRS,  $^1\text{H}$ -MRI using the Dixon technique and hyperpolarized  $^{13}\text{C}$ -MRS. A short overview of current and emerging applications is provided.

## GENERAL CONSIDERATIONS FOR THE PERFORMANCE OF CARDIAC MRS

Cardiac MRS and MRI are highly challenging as a result of cardiac and respiratory motion and field inhomogeneities. Several methods have been developed for cardiac shimming and to compensate for cardiac and respiratory motion.

### $B_0$ and $B_1$ field homogeneities

Most human studies on cardiac MR are currently performed at a magnetic field strength ( $B_0$ ) of 1.5 or 3 T (22), although promising results for  $^{31}\text{P}$ -MRS have been reported at 7 T (23). *In vivo* animal studies are performed at field strengths up to 11.7 T (24). It is well known that cardiac MRI at higher  $B_0$  field improves the signal-to-noise (SNR) and contrast-to-noise (CNR) ratios as a result of increased magnetization in humans (25) and animals (26).

Likewise, cardiac spectroscopy at higher  $B_0$  field benefits from improved SNR. Challenges at higher field strength include increased  $T_1$  relaxation time, inhomogeneous  $B_0$  and  $B_1$  fields, increased specific absorption rate (SAR) and degradation of the electrocardiogram (ECG). At higher  $B_0$  field, susceptibility effects increase, leading to stronger field distortions at interfaces between tissue and air, such as the heart-lung interface (27). In MRS, field inhomogeneities lead to broadened peaks. It should be noted that  $B_0$  challenges of high-field cardiac MRS in small rodents are smaller than in humans because of the smaller volume of interest (VOI) in small animals, and thus smaller field inhomogeneities in a relatively small VOI. However, with an increase in  $B_0$  field strength, the resonance frequency increases, leading to an improved separation of spectral peaks. In a human study, it has been shown that increased spectral resolution and improved SNR lead to improved quantification of myocardial fat peaks at 3 T compared with 1.5 T (28).

Cardiac shimming is complicated by phase shifts caused by cardiac and respiratory motion and blood flow. To overcome this, different shim methods have been developed, i.e. general and cardiac-specific shim methods. Shimming can be performed manually, which is time consuming and requires operator experience. Manual shimming is more often used in experimental animals [e.g. refs. (29,30)], but also automated shimming procedures can be used in preclinical studies [e.g. ref. (31)]. Most shimming procedures used for human applications are currently automated, such as shimming based on magnetic field mapping ( $B_0$  mapping) (32). The  $B_0$  mapping time can be reduced, e.g. by using linear projection mapping (33). The first cardiac-specific shim method, based on  $B_0$  mapping using chemical shift imaging (CSI), was introduced by Jaffer *et al.* (34). The CSI dataset was obtained throughout multiple cardiac and respiratory cycles, and a time- and motion-averaged  $B_0$  map of the heart was calculated. Later, it was shown that cardiac ECG-triggered and respiratory-gated local linear shimming improved the shim quality (35). More recently, it has been shown that  $B_0$  mapping using a three-dimensional (3D) cardiac-triggered gradient-echo sequence during consecutive breath-holds, followed by first-order cardiac phase-specific shimming, leads to an average gain in field homogeneity of 10% (36). A drawback is that ECG triggering during  $B_0$  map estimation increases the acquisition time. It has been shown that low-resolution field maps for cardiac shimming can be acquired during a breath-hold of 8–10 s without ECG triggering, yielding negligible temporal variation over the cardiac cycle (37).

Cardiac MRS and MRI at high field ( $\geq 3$  T) not only suffer from increased magnetic field inhomogeneity, but also from transmit radiofrequency (RF) ( $B_1$ ) field inhomogeneities. Schär *et al.* (38) have shown in humans that combined acquisition of  $B_0$  and  $B_1$  maps is feasible within one single breath-hold using a cardiac-triggered, modified, saturated double-angle method (SDAM) (39). Using this method, localized shim,  $f_0$  and RF power settings can be derived (38).

### Coils

The RF coil is an essential component of the MR system for RF excitation and signal reception. For  $^1\text{H}$ -MRS, usually the same RF coils can be used as for MRI. RF volume coils are mostly used for signal transmission because of their high  $B_1$  field homogeneity and can also be employed as receive coils. Cardiac  $^1\text{H}$ -MRS studies in humans are usually performed using surface receive-only coils,



which is advantageous in terms of SNR. In cardiac  $^1\text{H}$ -MRS animal studies, volume coils (send and receive), as well as surface receive coils, are currently used.

$^{31}\text{P}$ - and  $^{13}\text{C}$ -MRS require dedicated  $^{31}\text{P}$  and  $^{13}\text{C}$  coils and a second (multi-nuclei) RF channel. For  $^{31}\text{P}$ - and  $^{13}\text{C}$ -MRS studies, frequently surface coils are used as transmit/receive coils. As the transmit coil needs to produce a homogeneous  $B_1$  field in the VOI and the exact position of the VOI is usually not known in advance, the size of the surface transmit coil is usually relatively large (40).

The diameter of the surface receive coil must be chosen to be roughly equal to the depth of the organ of examination (41). Therefore, a surface receive coil of around 10 cm in diameter will mostly suffice for cardiac MRS in humans. Careful positioning of the surface coil is important to achieve the highest signal from the organ of interest. To this end, MRI is required to verify the position of the VOI.

Furthermore, dual-tuned coils, such as  $^1\text{H}/^{13}\text{C}$  coils or  $^1\text{H}/^{31}\text{P}$  coils, can be used. Dual-tuned coils require two channels and can also be used for indirect detection of low-sensitivity nuclei. The advantage of indirect (proton-observed) detection is the increased sensitivity of  $^1\text{H}$  compared with  $^{13}\text{C}$  or  $^{31}\text{P}$  nuclei.

Finally, using multi-channel coils or phased-array receive coils, SNR can be further improved in cardiac MRS (42,43). However, the number of spectra to be processed is increased by a factor equal to the number of channels used for signal reception. To this end, several automated methods have been developed (44–46), of which the more recently whitened singular value decomposition has been shown to work in practice (47). Multi-channel coils also enable parallel imaging, thereby reducing the scan time, which is beneficial for the generally long cardiac examinations.

### Cardiac and respiratory motion compensation

Since the first cardiac MRS measurements *in vivo*, the effect of cardiac and respiratory motion on spectral quality has been recognized (48). To compensate for cardiac motion, cardiac ECG synchronization with prospective triggering is generally used in MRS (49), which requires a predefined time interval between the trigger and data acquisition. This interval can be determined from cine images in order to constrain the acquisition of spectra to end-systole or diastole, when cardiac motion is minimal. For reproducible measurement of cardiac  $^1\text{H}$ -MR spectra, it has been shown that respiratory motion correction is essential (50,51). Different methods can be used: breath-hold (52), respiratory gating using a pressure belt (18), gating based on respiration-related ECG amplitude modulation (53) and respiratory gating based on navigator echo signals (54). The use of (multiple) breath-holds limits the scan time. In healthy volunteers, it has been demonstrated recently that single-breath-hold  $^1\text{H}$ -MRS enables the reliable quantification of myocardial lipids (55). However, the use of (multiple) breath-holds may be difficult for cardiac patients and often leads to undesirable changes in heart rate. The quality of ECG-based respiratory motion correction is dependent on correct placement of the ECG electrodes, and the ECG signal is susceptible to interference from RF pulses and gradient switching. Using navigator-based respiratory motion compensation, the displacement of the diaphragm is measured and spectral data acquisition is allowed in a predefined window of the respiratory cycle. This method improves the spectral quality significantly (51). A disadvantage of the navigator technique is that changes

in breathing pattern can reduce gating efficiency, leading to long scan times. In humans, it has been shown that respiratory motion compensation using an abdominal pressure belt yields comparable results to respiratory motion compensation using navigator signals (56). Furthermore, prospective volume tracking based on multiple navigator echoes can be used to compensate for respiratory motion. Using the volume tracking technique, an improved spectral quality was found compared with non-navigated reference acquisitions in humans (57).

The MR examination of animals *in vivo* requires the use of anesthesia, body temperature support and physiological monitoring. This can be achieved using MR-compatible devices, which are commercially available. To minimize motion artifacts, routine triggering to the R-peak of the ECG signal is used. Therefore, a high-quality ECG signal is required. To avoid the degradation of ECG signals by RF pulses and gradient switching, the use of MR-compatible ECG electrodes is recommended. As a result of the high heart rates and often low ECG signals in small rodents, dedicated monitoring and gating systems have been developed. For respiratory motion correction in small animals, it is clear that breath-holds cannot be used. Respiratory motion can be detected noninvasively using an optical displacement sensor (58,59), a contactless infrared motion detector (60), a partial-body plethysmograph (61), a lever pickup coil (62), amplitude modulations of the ECG signal (63) or a respiratory belt with a pneumatic sensor. In most preclinical studies, the pneumatic sensor is used. When using the partial-body plethysmograph, access to the animal is restricted, which can be problematic, for instance by hampering the administration of hyperpolarized substrates (61). Respiratory motion detection based on amplitude modulation of the ECG signal requires correct placement of the electrodes and is liable to electromagnetic interference. The lever pickup coil relies on electromagnetic induction and therefore may suffer from inductive crosstalk with the resonator or gradients, which can cause artifacts in the lever coil signal (62). More recently, an optical fiber-based gating device has been developed, which simultaneously provides information on respiratory and cardiac movement for prospective cardiac MRI (64). It has been shown that this device performs similarly to the ECG and pneumatic sensor.

Cassidy *et al.* (65) tested the performance of different motion gating strategies for mice MR at 11.75 T. The motion gating strategies included no gating, cardiac gating, cardiac gating with blanking during respiration, automatic gating and user-defined gating. It was shown that user-defined gating with steady-state maintenance during respiration for mouse cardiac MRI and MRS yielded the best quality MR data compared with cardiac gating only.

### Spectral processing and quantification

Following spectral acquisition, spectral analysis needs to be performed for the identification and quantification of spectral peaks. Spectral fitting can be performed with dedicated software, such as LCModel (66) and jMRUI (67), and has been extensively reviewed by Poulet *et al.* (68). Metabolite concentrations are most often presented as ratios (e.g. relative to a reference peak). Alternatively, the absolute quantification of metabolites can be performed, as reviewed by Jansen *et al.* (69). For the absolute quantification of myocardial  $^{31}\text{P}$  metabolites, the phantom replacement method (70,71) and the external reference method (72) have been employed. For the absolute quantification of

cardiac phosphorus spectra, correction for nuclear Overhauser enhancement (NOE) is required (73). Furthermore, the coil sensitivity profile (74,75), local flip angle and partial volume effects (75) need to be taken into account. For both absolute and relative quantification, correction for blood contamination (76,77) and  $T_1$  saturation when TR is short (e.g. smaller than five times the  $T_1$  relaxation time) (78) is required. As relative quantification is less time consuming and less prone to errors, it is still mostly used in cardiac  $^{31}\text{P}$ - and  $^1\text{H}$ -MRS, e.g. when determining the PCr/ATP ratio as a measure of cardiac energy status or the  $\text{CH}_2/\text{H}_2\text{O}$  ratio as a measure of cardiac lipid content.

## SPECTROSCOPY OF CARDIAC METABOLISM

MRS can be used to detect noninvasively metabolites with  $^{31}\text{P}$ ,  $^1\text{H}$  or  $^{13}\text{C}$  nuclei in the heart. In order to perform MRS on a clinical scanner, additional software and, for  $^{31}\text{P}$ - and  $^{13}\text{C}$ -MRS, additional hardware are required. The first *in vivo* cardiac metabolic investigations were performed using  $^{31}\text{P}$ -MRS to detect  $^{31}\text{P}$ -containing metabolites, followed by  $^1\text{H}$ -MRS and, more recently,  $^{13}\text{C}$ -MRS.

Tables 1 and 2 show the applications of cardiac MRS to study metabolism in cardiac diseases in humans and animals, respectively. These tables illustrate cardiac MRS applications and are a selection of a literature search performed in PubMed with the search criteria: 'in vivo, MRS / magnetic resonance spectroscopy, human / (guinea)pig / dog / rat / hamster / mice, heart / myocardium'. We included studies related to common metabolic diseases, such as type 2 diabetes mellitus (T2DM), different types of cardiomyopathy and heart failure, or to common conditions that can affect cardiac metabolism, such as aging and obesity. Studies focusing on very specific mutations or rare diseases were omitted.

### $^{31}\text{P}$ -MRS: ATP, PCr and inorganic phosphate (Pi)

Cardiac  $^{31}\text{P}$ -MRS is used for the detection of metabolites, such as ATP and PCr. In Fig. 1, the metabolites which can be detected using  $^{31}\text{P}$ -MRS are delineated by red boxes. An example of a cardiac phosphorous spectrum is given in Fig. 2. Phosphorus spectroscopy is generally used to assess cardiac energy status. The PCr/ATP ratio is a measure of cardiac energy status, because

**Table 1.** Applications of noninvasive cardiac MRS *in vivo* in myocardial disease: human studies

Nucleus	Metabolites of interest	Changes in/under pathological conditions
$^1\text{H}$ , relative sensitivity: 1*	TG	Aging (79), type 2 diabetes mellitus (80,81), obesity (52), impaired diastolic function (79,81) and increased left ventricular (LV) work (52) are conditions associated with increased myocardial TG Hypertrophic (82) and dilated (83) cardiomyopathy are associated with decreased myocardial TG content Ischemic cardiomyopathy is associated with increased myocardial TG content (82)
	Cr	Hypertrophic (82,84,85), dilated (82,84,85) and ischemic (82) cardiomyopathy, and (nonischemic) chronic heart failure (86), are conditions associated with decreased myocardial Cr content Higher LV ejection fraction is associated with increased myocardial Cr content (85)
$^{31}\text{P}$ , relative sensitivity: $\approx 1/15.04^*$	PCr/ATP ratio	Insulin sensitivity (87) and type 2 diabetes mellitus are associated with a decreased myocardial PCr/ATP ratio (88,89) • Decreased myocardial PCr/ATP ratio is not always found in patients with type 2 diabetes mellitus (90) PCr and ATP content are reduced in patients with ischemic heart disease (71,91) Ischemic heart disease/cardiomyopathy is associated with a decreased PCr/ATP ratio (76,92,93) • Similar PCr/ATP ratio can be found in viable myocardium and controls (94) • Akinetic myocardium shows no PCr peak (94) Non-ischemic dilated cardiomyopathy (72,95) and hypertrophic cardiomyopathy (96–99) are associated with a decreased PCr/ATP ratio • A decreased PCr/ATP ratio is associated with higher mortality in dilated cardiomyopathy (17) Heart failure with preserved ejection fraction is associated with reduced PCr/ATP ratio (100) • Beta-blockers (101) and trimetazidine (102) improve PCr/ATP ratio in patients with heart failure PCr/ATP ratio is reduced in young men with fatty liver (103)
	PCr/Pi ratio	Hypertrophic cardiomyopathy is associated with a decreased PCr/Pi ratio (104)
	ATP flux through CK reaction	LV hypertrophy (105), hypertrophic cardiomyopathy of genetic origin (106), myocardial infarction (107) and heart failure (108,105) are associated with a decreased ATP flux through CK reaction

\*The relative sensitivity indicates the MR sensitivity multiplied by the natural abundance of the nucleus.  
ATP, adenosine triphosphate; CK, creatine kinase; PCr, phosphocreatine; Pi, inorganic phosphate; TG, triglyceride.

**Table 2.** Applications of noninvasive cardiac MRS *in vivo* in animal models of myocardial disease: (guinea)pig/dog/rat/hamster/mouse

Nucleus	Metabolites of interest	Changes in/under pathological conditions
<sup>1</sup> H, relative sensitivity: 1*	TG	Cardiac lipid accumulation may be an early indication of the cardiovascular pathophysiology associated with type 2 diabetes in rats fed a high-fat diet (109) Cardiomyopathy is associated with decreased myocardial TG content in Syrian hamsters (110) Increased myocardial TG levels in mice coincide with compromised two-dimensional strain values in the left-ventricular (LV) wall (111) Fasting-induced myocardial TG accumulation in LCAD knockout mice correlates with impaired LV function (30)
	Cr	Chronically (up to two-fold) increased myocardial Cr levels in mice over-expressing the myocardial Cr transporter lead to progressive hypertrophy and heart failure (112) Myocardial Cr levels of approximately 100% above normal values in mice overexpressing the myocardial Cr transporter protect the heart from ischemia/reperfusion injury and myocardial stunning (113)
<sup>31</sup> P, relative sensitivity: ≈1/15.04*	PCr/ATP ratio	No change in PCr/ATP ratio is found in rats with streptozotocin-induced diabetes mellitus (114) High-fat diet-induced early-stage cardiomyopathy in mice is not associated with reduced myocardial PCr/ATP ratio (115) Hypertrophic cardiomyopathy in Syrian hamsters (110) and mice (116) is associated with a decreased PCr/ATP ratio Myocardial infarction in mice (117), rats (118), dogs (119) and swine (120) is associated with a reduction in PCr/ATP ratio, as well as ventricular remodeling <ul style="list-style-type: none"> <li>• Short-term (5-min) occlusion does not affect the PCr/ATP ratio in dogs (121)</li> <li>• Short-term (4 weeks) selective β1-blockade (118) and treatment with growth hormone (122) increase the PCr/ATP ratio during post-infarct remodeling</li> </ul>
	ATP flux through CK reaction	Chronic energy deficiency leads to cardiac dysfunction in mice and rats (31,123–125) The ATP synthesis rate through the CK reaction is reduced in mice with heart failure (126) A reduced ATP flux through the CK reaction contributes to contractile dysfunction (127)
<sup>13</sup> C, relative sensitivity: ≈1/5681.82*†	PDH activity and flux	Reduced PDH flux in rat heart correlates with the severity of type 1 diabetes mellitus (128) Reduced PDH flux may contribute to the development of cardiac hypertrophy in the hyperthyroid rat heart <i>in vivo</i> (129) Reduced PDH flux reveals the onset of overt heart failure in pig <i>in vivo</i> (130) Hypertensive rat hearts show an increase in PDH flux (131)
	TCA cycle activity	After myocardial infarction, TCA cycle activity is reduced. The reduction in TCA cycle activity correlates with the degree of cardiac dysfunction (132)

\*The relative sensitivity indicates the MR sensitivity multiplied by the natural abundance of the nucleus.

†The low relative sensitivity of <sup>13</sup>C is overcome by dynamic nuclear polarization (DNP) in the quoted references.

ATP, adenosine triphosphate; CK, creatine kinase; Cr, creatine; LCAD, long-chain acyl-CoA dehydrogenase; PCr, phosphocreatine; PDH, pyruvate dehydrogenase; TCA, tricarboxylic acid; TG, triglyceride.

any temporary mismatch between ATP demand and supply is met by the breakdown of PCr, catalyzed by the CK enzyme.

The relative MR sensitivity of phosphorus is about 15 times lower than that of a proton. However, there is no dominant signal that requires suppression to detect the peaks of interest (such as the water signal in <sup>1</sup>H-MRS). The phosphorus metabolite concentrations in healthy human heart have been reported to be 10.4 ± 1.5 μmol/g wet weight for [PCr] and 6.0 ± 1.1 μmol/g wet weight for [ATP] [all mean ± standard deviation (SD)] (133). The ATP concentration correlates well with values obtained from biochemical assays, but the PCr concentration obtained from biochemical assays may be less reliable as a result of rapid PCr loss during sampling (74,134). Cardiac applications of <sup>31</sup>P-MRS require the localization of the detected signal to minimize contamination from signal outside the VOI, especially from chest

muscle and liver. A typical voxel used for cardiac <sup>31</sup>P-MRS is placed over the heart and is approximately 5 × 6 × 6 cm<sup>3</sup> in humans. Furthermore, the typical duration of the acquisition of a cardiac phosphorus spectrum usually varies between 10 and 20 min. Several localization sequences have been developed. As a result of the short T<sub>2</sub> relaxation times of ATP and Pi, generally free induction decay (FID) localization methods are used, in which FID is measured immediately after excitation. Localization sequences used for cardiac <sup>31</sup>P-MRS include image-selected *in vivo* spectroscopy (ISIS) and CSI. Using 3D ISIS, cubic volumes can be selected by adding and subtracting eight FID MR signals (135), which are acquired with slice-selective inversion pre-pulses that are switched on and off along the three Cartesian axes. In the resulting FID signal, the signals from outside the cubic volume are canceled out. Localization using ISIS can be

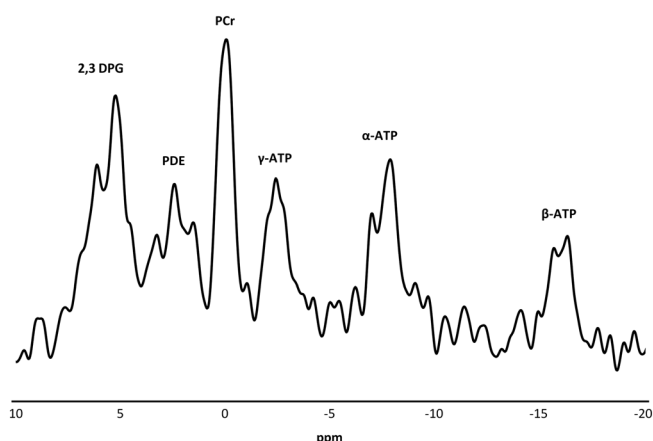


**Figure 2.** Example of a cardiac phosphorus ( $^{31}\text{P}$ ) spectrum obtained from a healthy volunteer at a clinical 1.5-T scanner. The shimming volume and three-dimensional (3D) image-selected *in vivo* spectroscopy (ISIS) volume ( $\text{TR} = 3.6$  s; number of averages, 192) were positioned over the entire left ventricle. Electrocardiogram (ECG) triggering was performed to reduce motion artifacts. As the 3D ISIS volume included the entire left ventricle, a large amount of signal also originates from blood, which is evidenced by the prominent 2,3-DPG peak. The PCr/ATP ratio in this subject was 2.35. The metabolite peaks are indicated in the spectrum. 2,3-DPG, 2,3-diphosphoglycerate; ATP, adenine triphosphate; PDE, phosphodiester; PCr, phosphocreatine.

hampered by motion, because of disturbance of the differencing scheme. When using single-voxel localization techniques, such as ISIS, one must also be aware that a chemical shift displacement artifact can occur. 1D-, 2D- and 3D CSI, with phase encoding in one, two and three dimensions, allows the selection of multiple voxels for spectroscopic analysis during a single measurement, at the expense of longer scan times. The nominal voxel size is determined by the number of phase-encoding steps in a chosen field of view. However, the actual voxel size is also determined by the point spread function and is therefore larger than the nominal voxel size and also contains signal from other voxels. CSI can be combined with other spatial localization techniques, such as ISIS. At a 1.5-T scanner, it has been shown that the PCr/ATP ratios using 3D localization techniques (3D ISIS and a combination of 2D ISIS and 1D CSI) are comparable, but significantly lower PCr/ATP ratios are obtained using 1D CSI (136). The lower PCr/ATP ratio with the less well-defined localization by 1D CSI may be a result of contamination of cardiac spectra by liver tissue and/or skeletal muscle. As a result of the negative lobe of the point spread function, high PCr signal originating from skeletal muscle may be subtracted from the signal obtained from the heart. In addition, a reduction in the PCr/ATP ratio may also partly be explained by contamination of blood, which would add ATP signals, but no PCr. Blood contamination can be corrected for using the 2,3-diphosphoglycerate (2,3-DPG) signals (76). Furthermore, large differences in PCr/ATP ratio were observed between serial examinations (with a time interval of 7 days) for all localization techniques in humans (136). At a 3-T scanner, good reproducibility with a variance of 12% was found when measuring the PCr/ATP ratio using ISIS volume selection in subjects on both the same day and on different days (96). To allow matching of the shape and size of the sensitive volume to the anatomy of the subject, thereby reducing contamination from

adjacent organs and improving sensitivity, spatial localization with optimal point spread function (SLOOP) was developed (137). Compared with CSI, the SNR was improved by approximately 30% using SLOOP (138).

It is also feasible to determine absolute concentrations of metabolites with cardiac  $^{31}\text{P}$ -MRS (70,71,116). Absolute quantification has the advantage that it is unaffected by concentration changes of the reference metabolite. For absolute as well as relative quantification, several effects must be corrected for, including  $T_1$  saturation (78) as described above. In several studies on murine cardiac energy status, an ISIS sequence was used for localized cardiac  $^{31}\text{P}$ -MRS. In one study, the localized volume was placed over the entire heart (139). In other studies, the localized volume enclosed only the left ventricle (123,124,115). At higher magnetic field strengths, spectroscopic data can be acquired with higher spatial resolution. The feasibility of 1D CSI for the measurement of the cardiac energy status of the anterior wall was shown at 4.7 T, and the measured PCr/ATP ratios in mice were similar to the values reported in humans ( $2.0 \pm 0.2$ ) (140). Thereafter, several studies on murine cardiac energy status were performed using 1D CSI, e.g. refs. (116,125,117). With a further increase in magnetic field strength, the feasibility of high-spatial-resolution 2D CSI (voxel size, 21–28  $\mu\text{L}$ ) for the examination of murine cardiac energy status has been shown at 9.4 T (141). However, the total acquisition time was around 75 min when using 2D CSI compared with around 34 min when using 1D CSI (140,141).

### $^{31}\text{P}$ -MRS: results from human studies

The PCr/ATP ratio has been shown to be reduced in dilated cardiomyopathy in most (72,76,95), but not all (142), studies. Later, it was shown in patients with heart failure as a result of dilated cardiomyopathy that a low PCr/ATP ratio is a predictor of cardiovascular mortality (17). Although Pi cannot usually be determined because of the overlapping resonances from 2,3-DPG originating from blood, the quantification of Pi has been reported with a specifically optimized protocol, using decoupling and NOE in combination with small voxels (achieved by spectroscopic imaging). This results in limited contamination of blood, especially in patients with cardiomyopathy with severely dilated hearts. In patients with dilated cardiomyopathy, a decreased PCr/Pi ratio has been shown using this method (104). A reduced PCr/ATP ratio was found in hypertrophic cardiomyopathy (96–99), heart failure with preserved ejection fraction (100), ischemic heart disease (71,92) and subacute myocardial infarction (94,93). In patients with old myocardial infarction, only reduced ATP and PCr values were found (91). It has been shown that beta-blockers (101) and trimetazidine (102) (a fatty acid oxidation inhibitor), in addition to improving left ventricular function, also improve the cardiac PCr/ATP ratio in patients with heart failure. The PCr/ATP ratio has also been shown to be reduced in individuals with fatty liver (103) and in patients with T2DM with high liver TG content (143). In addition, impaired insulin sensitivity (87) and T2DM are associated with decreased PCr/ATP ratio in some (88,89), but not all (90), studies. Interestingly, the resting heart rate was found to be inversely associated with PCr/ATP ratio in healthy young men (144) and a correlation between maximal working capacity and myocardial PCr/ATP ratio was found in healthy male volunteers ( $n = 105$ ) (145). Acute exercise does not seem to affect the PCr/ATP ratio in healthy subjects, independent of the training status, as the PCr/ATP ratio remained unchanged



when trained and untrained ( $n = 12$ ) volunteers were performing exercise inside the scanner (146,147). However, under high-level pharmacological stress conditions, a reduction in myocardial PCr/ATP ratio was reported (148). Lower pharmacologically induced stress levels did not have this effect in healthy volunteers or in patients with dilated cardiomyopathy (149).

### <sup>31</sup>P-MRS: results from animal studies

For the first cardiac MRS studies, mainly large animals, such as dogs and pigs, were used. Usually, pigs are preferred to dogs, as the size and cardiovascular of a pig heart closely resembles the human situation (150,151). Most cardiac MRS experiments performed in dogs and pigs were highly invasive, as the chest was opened and a surface coil was sutured onto the epicardium, e.g. refs. (152–156). However, it has been shown that results from experiments performed in closed-chest dogs are in accordance with results from experiments performed in open-chest dogs (157,158), thereby paving the way for longitudinal studies. After the onset of 5-min occlusion and during 30 min of reperfusion therapy, no change in PCr/ATP ratio was found in dogs (121). In swine, it has been shown that the PCr/ATP ratio is reduced at 4 weeks post-myocardial infarction (120). In canine myocardium, it was shown, using a combination of <sup>1</sup>H- and <sup>31</sup>P-MRS, that CK metabolism is reduced after myocardial infarction (119). Both MRS and biopsy measurements showed infarct-related reductions in high-energy phosphates (119). A transmural change in PCr/ATP ratio and PCr content was shown in dogs, where the PCr/ATP ratio and PCr content were lower in the subendocardium relative to the subepicardium (159). The gradient in PCr/ATP ratio was shown not to be an artifact of the technique. In the same study, it was shown that the PCr/ATP ratio remains constant during the cardiac cycle.

Later, cardiac energy metabolism was also studied in small experimental animals *in vivo* (139,140). Noninvasive <sup>31</sup>P-MRS in small animal models *in vivo* is challenging because of the high heart rates and respiratory motion, as well as the small size of the heart in general. Nevertheless, several studies have been performed in small animal models of disease. It has been demonstrated that murine myocardial PCr/ATP ratios are similar to those in larger species, including humans, also during a pharmacologically induced increase in cardiac work (160). In murine hearts with pressure-overload hypertrophy induced by transverse aortic constriction, reductions in PCr/ATP ratio and ATP concentration were found (116). This means that, under conditions of pressure-overload hypertrophy, mechanisms which normally replete the ATP pools are inadequate. It has been shown that the relationship between abnormal energetics and contractile dysfunction and ventricular geometry changes over time in pressure-overload hypertrophy. The early abnormal energetics in mice predict the extent of contractile dysfunction and subsequent ventricular remodeling (125). In addition, in Syrian hamsters, it has been shown that myocardial PCr/ATP levels start to decrease at the hypertrophic stage of cardiomyopathy and further decrease at the congestive stage of the disease (110). The model of pressure-overload hypertrophy thus provides insights into the causes and consequences of hypertrophy. Moreover, the observation that the relationship between cardiac energy status and contractile function varies over time may be important for the interpretation of human data on this topic, as it shows that the relationship between the PCr/ATP ratio and contractile function is complex.

As described previously, a reduction in PCr/ATP ratio and ventricular remodeling are also observed after myocardial infarction. Clinical deterioration after myocardial infarction has been associated with increased levels of serum uric acids and raised reactive oxygen species (161). It has been shown that supplementation of a xanthine oxidase inhibitor, which reduces serum uric acid and oxidative stress, after myocardial infarction reverses the process of ventricular remodeling, together with a normalization of the PCr/ATP ratio in mice (117). Therefore, this rodent study supports the energy starvation hypothesis of heart failure, showing that normalized energetics coincide with improved contractile function. In addition, in rats with myocardial infarction, it has been shown using <sup>31</sup>P-MRS that cardiac bioenergetics during early post-infarct remodeling improve by selective  $\beta$ -blockade (118). The improvement in cardiac energetics was associated with an improvement in left ventricular function. However, long-term selective  $\beta_1$ -blockade in a rat model of post-infarction congestive heart failure attenuated remodeling, but did not improve myocardial energy metabolism and left ventricular function (162). The mechanisms of action of  $\beta$ -blockade are not fully understood. Furthermore, it has been shown that treatment with growth hormone after myocardial infarction improves the myocardial energetics, possibly by protecting the myocardium from the adverse effects of catecholamines (122). In contrast, transgenic mice with selective bovine growth hormone overexpression in the brain, which resulted in lower myocardial catecholamine content, showed decreased PCr/ATP ratios in the heart (163). Interestingly, pretreatment with verapamil (which is known to exert vasodilatory effects) in rats before myocardial ischemia and reperfusion has been shown to exert a protective effect, as it leads to a higher degree of PCr recovery after 60 min of reperfusion (163). PCr recovery has been shown to be inversely correlated with infarct size (164).

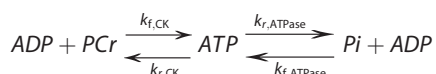
As  $\beta$ -oxidation of LCFAs provides the major energy source of the heart, disturbances in fat oxidation can lead to cardiac dysfunction. For example, deficiency in mitochondrial very-long-chain acyl-CoA dehydrogenase (VLCAD), which catalyzes the first step in  $\beta$ -oxidation, leads to a reduction in myocardial fatty acid  $\beta$ -oxidation and energy production. It has been demonstrated recently in VLCAD knockout mice that chronic energy deficiency leads to cardiac dysfunction, which cannot be effectively improved using dietary supplementation of medium-chain TGs (31). Long-chain acyl-CoA dehydrogenase (LCAD) knockout mice show a similar phenotype to humans deficient in VLCAD in the fasted condition. In the fasted condition, where the heart normally is most reliant on fatty acid oxidation, an impairment in myocardial energy status has been demonstrated with <sup>31</sup>P-MRS in LCAD-deficient mice, eventually leading to impaired cardiac performance (124).

In addition, in rats, it has been shown, using <sup>31</sup>P-MRS, that Cr depletion results in disturbed energy metabolism, as exemplified by a reduced PCr/ATP ratio, compromised left ventricular function and remodeling (123). However, in a mouse model of high-fat diet-induced obesity, no reduction in PCr/ATP ratio was found, whereas diastolic function was reduced (115). It was suggested in this study that lipotoxicity-induced fibrosis, as well as lipotoxicity-induced oxidative stress, which may disturb calcium homeostasis, may contribute to diastolic dysfunction, rather than impaired cardiac energetics.

Similarly, in rats with streptozotocin-induced diabetes mellitus, no change in PCr/ATP ratio was found, whereas early cardiac dysfunction was observed (114).

### <sup>31</sup>P-Magnetization transfer spectroscopy (<sup>31</sup>P-MTS): fluxes through the CK reaction

Using MTS, the reaction rate and flux through the CK reaction in heart muscle can be measured. When the rate constant of the CK reaction is multiplied by the PCr concentration, the (forward) CK flux is obtained. An example of a cardiac <sup>31</sup>P-MTS spectrum is given in Fig. 3. The generation of ATP is largely controlled by the CK and ATP synthase enzymes. The CK enzyme catalyzes the conversion from ADP and PCr to ATP. The ATP synthase enzyme catalyzes the conversion from ADP and Pi to ATP:



Under most *in vivo* conditions, the forward and reverse fluxes for CK and ATPase are equal (165). In MTS, the signal of a target molecular subunit (e.g.  $\gamma$ -ATP) can be saturated by a saturation pulse, and transfer of the saturated signal through chemical exchange (e.g. to PCr) is measured to determine the chemical exchange rate. Saturation transfer is most commonly used but, alternatively, magnetization transfer can also be achieved using a frequency-selective inversion pulse. In a saturation transfer experiment, the spins are first allowed to reach steady-state equilibrium during the preparation period. The preparation period is followed by the mixing period, in which chemical-selective irradiation takes place to saturate the  $\gamma$ -ATP signal. As a consequence, a reduction in the PCr signal ( $M'$ ) from its equilibrium value ( $M_0$ ) can be observed (166). To calculate the reaction rate and flux, measurement of  $M'$  and  $M_0$  is required, as well as the spin-lattice relaxation time  $T_1'$  of PCr when  $\gamma$ -ATP is saturated, and the intracellular PCr concentration. These requirements to calculate the reaction rate and flux lead to long acquisition times. As a result of the long acquisition times [up to 6 h (167)], MTS was initially not practical for human research. To overcome these long acquisition times, several adaptations to the acquisition have been made. First, some studies were performed in which  $M_0'$  and  $M_0$  were acquired under partially saturated conditions (168). When measuring under partially saturated conditions, there are some pitfalls, as discussed in refs. (169–171). Nonlocalized measurements were performed for reasonably fast  $T_1'$  and  $T_1$  estimation (172,173), assuming no spatial variation in  $T_1'$ ,  $T_1$  and, consequently, in  $M'$  and  $M_0$ . To compensate for the partial saturation, different correction methods were employed. Hsieh and Balaban (174) compensated for short TR ( $\text{TR} < 5T_{1\text{app}}$ ) by

calculating the saturation factor. In the meantime, the dual-angle method for nonlocalized  $T_1$  determination using low-angle adiabatic pulses by Bottomley and Ouwerkerk (175) paved the way for faster assessment of  $T_1$ . Using the dual-angle method for  $T_1$  determination together with chemical selective irradiation and control irradiation, the four-angle saturation transfer (FAST) method was created, in which the rate constants were determined in only four acquisitions (176). More recently, the ongoing dual-angle method (O-DAM) correction for partial saturation was introduced and was shown to be superior to conventional approaches (177). Using the O-DAM method,  $T_1$  measurements are performed throughout the course of an experiment. Using 1D CSI combined with the FAST method in human cardiac <sup>31</sup>P-MTS, a total acquisition time of 38–70 min was achieved (108,105). To further reduce the acquisition time, Xiong *et al.* (178) introduced a strategy in which optimized presaturation delays are calculated and the acquisition of only three spectra is required. The method yields a reduction of 82% in data acquisition time as compared with the conventional method. More recently, Xiong *et al.* (179) proposed a superfast magnetization transfer method in which only the acquisition of two spectra is required, yielding a reduction of 91% in data acquisition time as compared with the conventional method.

Recently, the reproducibility of <sup>31</sup>P saturation transfer MRS of the forward CK reaction in human heart was demonstrated, yielding a CK reaction rate constant of  $0.32 \pm 0.05 \text{ s}^{-1}$  and a coefficient of variation of 15.6% (180).

### <sup>31</sup>P-MTS: results from human studies

Decreased *in vivo* ATP production rates via the CK reaction have been associated with mild to moderate heart failure (108), left ventricular hypertrophy, chronic heart failure (105) and myocardial infarction (107) in humans (see Table 1). Furthermore, in hypertrophic cardiomyopathy of genetic origin, a reduced ATP production rate through the CK reaction has been found (106).

### <sup>31</sup>P-MTS: results from animal studies

It has been demonstrated that ATP synthesis through the CK reaction in the myocardium of mice is reduced in long-standing pressure overload and heart failure induced by thoracic aortic constriction (126). Later, a causal relationship between CK-related energy metabolism and contractile function in heart failure was demonstrated in a transgenic mouse model of myocardial

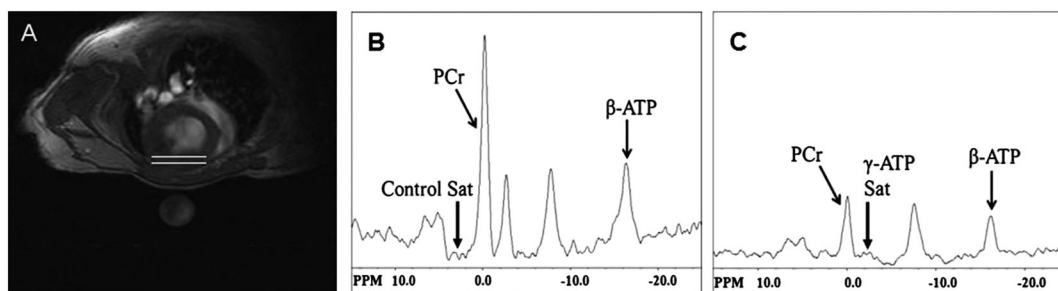


**Figure 3.** *In vivo* measures of myocardial energetics in doxorubicin administered mouse hearts were obtained with noninvasive <sup>31</sup>P MRS. (A) Typical transverse <sup>1</sup>H MR image of a mouse at the mid-left ventricle with the location of <sup>31</sup>P MR cardiac voxel denoted between the white lines. (B) <sup>31</sup>P MR spectrum with control saturation and TR=10s and number of excitations (NEX)=16. (C) Spectrum with  $\gamma$ -phosphate of ATP saturated with TR=6s, number of excitations=32. Reproduced from ref. (127) [Gupta A *et al.* (2013) Creatine kinase-overexpression improves myocardial energetics, contractile dysfunction and survival in murine doxorubicin cardiotoxicity. *PLoS One* 8(10): e74675. doi: 10.1371/journal.pone.0074675].

CK overexpression (127). Therefore, it has been suggested that CK may be a promising target for the treatment of heart failure.

### pH measurement

Measurement of pH using  $^{31}\text{P}$ -MRS is complicated because of overlap from 2,3-DPG originating from blood with the Pi peak, and therefore MTS can be used as an alternative. The application of a saturation pulse at the  $\gamma$ -ATP resonance frequency will reduce the intensity of the PCr and Pi peaks. Subtracting a control spectrum from the saturated spectrum yields a difference spectrum in which only signals from the phosphorus atoms which are in exchange with the  $\gamma$ -ATP pool are visible. Using the difference spectrum, the resonance frequency of the Pi peak relative to the PCr peak can be measured to determine pH, as shown in experimental animals and humans (181,182).

### $^1\text{H}$ -MRS: TG and total Cr

Cardiac  $^1\text{H}$ -MRS is used mostly for the detection of myocardial TG and total Cr, which are indicated in Fig. 1 by the blue boxes and arrows. In addition, the myocardial TG peak may also contain contributions from lactate, although the lactate peak cannot be distinguished from myocardial TG in the spectra that have been presented (183). A cardiac proton spectrum is shown in Fig. 4. The methyl resonance of total Cr (i.e. free Cr plus PCr), with its resonance frequency at 3.02 ppm (184,185), has a lower signal than the protons from the terminal methyl groups and the methylene chain of TGs, with resonance frequencies at 0.85 and 1.26 ppm, respectively (29,186). The most prominent signal is from water at 4.7 ppm. Myocardial total Cr and TG concentrations in healthy subjects have been reported to be  $27.1 \pm 4.3$  and  $4.05 \pm 1.94 \mu\text{mol/g}$  (all mean  $\pm$  SD), respectively (82). In humans, it has been shown that myocardial TG concentration is related to gender (187) and subject to diurnal variation (188). In general,  $^1\text{H}$  metabolites have longer  $T_2$  relaxation times compared with  $^{31}\text{P}/^{13}\text{C}$  metabolites, and therefore spin-echo sequences are generally used for the detection of  $^1\text{H}$  nuclei. The most frequently used single-voxel sequences for cardiac  $^1\text{H}$ -MRS are stimulated echo acquisition mode (STEAM) (189) and point-resolved spectroscopy (PRESS) (190). An advantage of the STEAM pulse sequence is that a shorter TE can be achieved than when using the PRESS pulse sequence. Consequently, using STEAM, the signal intensities of spectral peaks are less affected by  $T_2$  decay, which makes STEAM advantageous for the detection of metabolites with short  $T_2$  relaxation times. A disadvantage of the STEAM pulse sequence is that the amplitude of the acquired stimulated echo is theoretically only 50% of the acquired amplitude of the spin-echo compared with the PRESS pulse sequence when an equal TE is used. This means that the SNR of STEAM is usually lower than that of PRESS when the number of acquisitions is equal. From brain research, it is known that PRESS and STEAM have different sensitivity to  $J$ -coupling, which may affect the peak amplitudes. Therefore, it is recommended to use STEAM with short TE for the detection of coupled spins (191). It has also been shown that the PRESS sequence is relatively insensitive to physiological motion compared with STEAM (192). As, during the STEAM and PRESS pulse sequences, four unwanted echo signals and three unwanted FID signals are formed, phase cycling and/or crusher gradients need to be applied to remove these signals. The performance of phase cycling

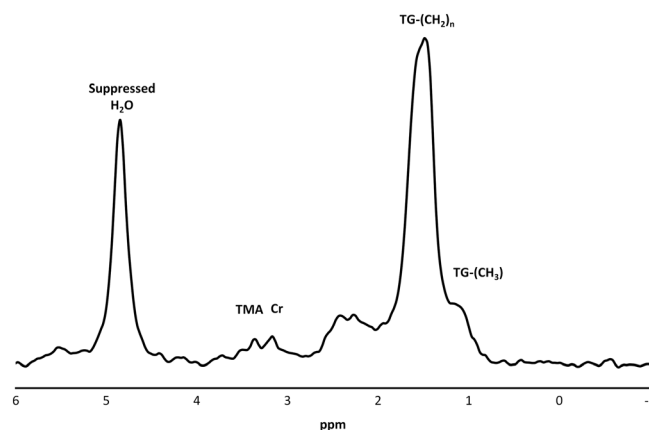


**Figure 4.** Example of a cardiac proton ( $^1\text{H}$ ) spectrum obtained from the septum of the heart from a healthy volunteer using a point-resolved spectroscopy (PRESS) sequence at a clinical 1.5-T scanner. The  $\text{H}_2\text{O}$  peak is partially suppressed using a chemical shift-selective water suppression (CHESS) module. The metabolite peaks include: TMA, trimethyl-ammonium compounds; Cr, creatine,  $\text{TG}-(\text{CH}_2)_n$ , triglyceride  $-(\text{CH}_2)_n$ ;  $\text{TG}-(\text{CH}_3)$ , triglyceride terminal methyl.

can be affected by motion (166). It has recently been demonstrated that the SNR of the PRESS sequence can be improved by reduction of the crusher area and an optimal timing of the trigger delay (193).

To detect myocardial TG and total Cr content, water suppression is required. A frequently used water suppression technique is chemical shift-selective water suppression (CHESS) (194). Conventional water suppression saturation pulses can influence the visibility of the Cr peak, thereby leading to underestimation of the Cr concentrations (195). In addition, it has been suggested that, depending on the TE used, not all the cardiac Cr may contribute to the  $^1\text{H}$ -MRS resonance at 3.02 ppm, possibly as a result of the compartmentation of Cr into pools (195).

The metabolite content is generally quantified relative to the water signal. Therefore, two spectra are acquired from the same voxel in the myocardium: a water-suppressed and a water-unsuppressed spectrum. To prevent contamination from epicardial fat, a voxel is generally positioned in the interventricular septum. This means that the voxel size in humans is limited to  $6\text{--}8\text{ cm}^3$  (18,82,79), whereas the voxel size in mice is approximately  $2\text{--}4\text{ mm}^3$  (29,30). When the voxel size is larger than the wall thickness, the spectrum may also include water signal from blood, which causes an underestimation of metabolite concentrations. Myocardial fat distribution may be heterogeneous in cardiovascular disease (196), and thus septal TG content may not represent the severity of global cardiolipectotoxicity (197). When the voxel is positioned at the myocardial wall, contamination from epicardial fat could lead to overestimation of the measured TG content (18). The scan duration for fast acquisition of a myocardial  $^1\text{H}$  MR spectrum varies between 4 and 8 min in humans.

CSI can be used for the detection of regional differences in myocardial TG and Cr contents, but the main limitation is the long scan duration. Recently, it has been shown that the fast echo-planar spectroscopic imaging (EPSI) sequence can be applied in the heart to measure the regional TG and Cr content in healthy volunteers (196). In this study, TG and Cr were measured in six regions of interest located in the midcavity region of the heart and compared with results from a single-voxel PRESS

spectrum obtained from the septal wall region. Results were found to agree well, but some regional variance across the EPSI data was found in the lateral region, which was attributed in part to reduced coil sensitivity and loss of spectral resolution as a consequence of line broadening caused by  $B_0$  inhomogeneity close to the posterior vein of the left ventricle (see also Fig. 5).

The correlation of TG methylene levels determined using  $^1\text{H}$ -MRS with biochemical measurements of total TG in rats has been shown to be good ( $r^2=0.94$ ,  $p<0.001$ ) (18). Also, in mice, TG methylene levels measured with *in vivo*  $^1\text{H}$ -MRS showed good correlation with biochemical measurements of total TG ( $r=0.91$ ,  $p<0.0001$ ) (30). In addition, tissue from human biopsy samples from 10 patients with severe aortic stenosis stained with Oil Red O for lipid quantification showed significant correlation with myocardial TG content as measured using *in vivo*  $^1\text{H}$ -MRS ( $r_s=0.66$ ,  $p=0.036$ ) (198). Furthermore, *in vivo* measurements showed good correlation ( $r^2=0.97$ ,  $p<0.005$ ) with *ex vivo* measurements performed on biopsy samples using magnetic angle spinning MRS and high-resolution MRS (199). Reproducible assessment of myocardial TG is improved by combined cardiac and respiratory triggering (200).

Although Cr may not be completely MR visible, it has been shown that total Cr values obtained with  $^1\text{H}$ -MRS in the myocardium of six dogs agreed well with total Cr values obtained from biopsy assays (201).

#### TGs: results from human studies

Myocardial TG accumulation in humans has been associated with aging (79), diabetes (80,81) and obesity (52). It has been shown that  $^1\text{H}$ -MRS is sufficiently sensitive to detect changes in myocardial TG content as a result of fasting and caloric restriction (202,203). Myocardial TG accumulation has been suggested to be an independent predictor of diastolic and systolic dysfunction (52) (see Table 1). Cardiac function has been shown to be improved in a group of subjects with obesity (204) and T2DM

(205) in interventions reducing cardiac TG content. In addition, in patients with hypothyroidism after levothyroxine treatment, a reduced cardiac lipid content, together with an improvement in cardiac function, was found (206). However, reducing cardiac TG content does not always improve cardiac function (207). Moreover, although increased myocardial TG content was found in patients with ischemic cardiomyopathy, patients with hypertrophic cardiomyopathy (82), as well as those with dilated cardiomyopathy (83), showed decreased myocardial TG content.

#### TGs: results from animal studies

To investigate mechanisms associated with myocardial TG accumulation, experimental animals have also been used. It has been shown in mice with cardiac-specific overexpression of peroxisome proliferator-activated receptor  $\alpha$  (PPAR $\alpha$ ) after exposure to a high-fat diet that increased myocardial TG levels coincide with compromised 2D strain values in the left ventricular wall (111). In mice deficient for LCAD, which catalyzes the first step in mitochondrial fatty acid  $\beta$ -oxidation, it was shown that, during fasting, increased myocardial TG accumulation is accompanied by impaired left ventricular function (30). These results point towards adverse effects of increased lipid levels in the myocardium. As a result of LCAD deficiency, reduced levels of free carnitine are found in LCAD knockout mice. Recently, it was shown that carnitine supplementation can be used to restore myocardial free carnitine levels, followed by normalization of total fatty acid content in LCAD knockout mice (208).

In rats exposed to a high-fat diet, cardiac lipid accumulation has been shown, together with moderate diabetes and mild cardiac hypertrophy (109). The cardiac lipid accumulation may be an early indication of the cardiovascular pathophysiology associated with type 2 diabetes. However, not all models of cardiac disease are characterized by TG accumulation. In Syrian hamsters, it was shown that cardiomyopathy is associated with decreased myocardial TG levels (110).

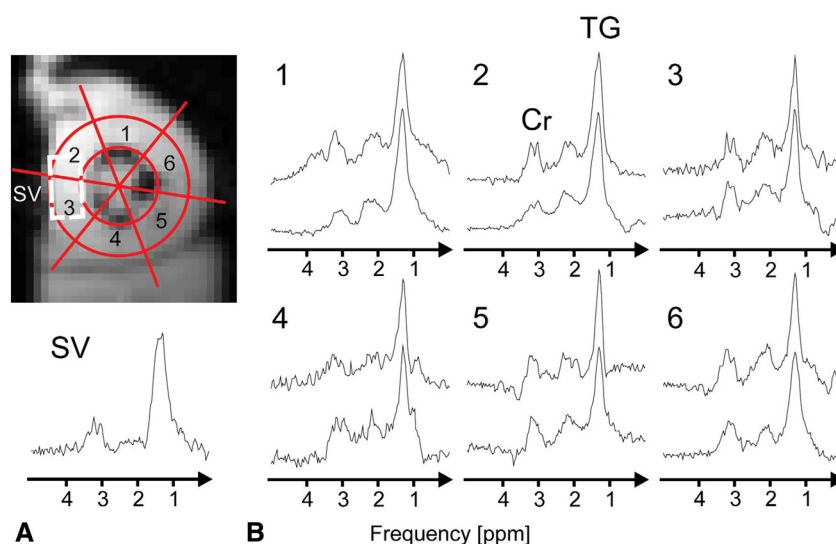


**Figure 5.** (A) Point-resolved spectroscopy (PRESS) (single voxel, SV) and echo-planar spectroscopic imaging (EPSI) regions of interest indicated in the EPSI reference scan. (B) Spectra from the regions of interest indicated in (A). To illustrate the reproducibility of the EPSI scans, two spectra from a single subject are shown for every segment. In all spectra, the triglyceride (TG) resonance at 1.3 ppm and the creatine (Cr) resonance at 3.01 ppm can be clearly seen. For comparison, a PRESS (SV) spectrum is shown. Reproduced from ref. (196) [Weiss K, Martini N, Boesiger P, Kozerke S. Metabolic MR imaging of regional triglyceride and creatine content in the human heart. *Magn. Reson. Med.* 2012; 68: 1696–1704. Copyright (c) 2012 Wiley Periodicals, Inc.].



### Cr: results from human studies

In cardiac energy metabolism, the CK system is essential as it is involved in ATP synthesis. Sufficient cardiac Cr levels are important to maintain the capacity of the CK system. Total myocardial Cr levels, i.e. free Cr plus PCr, can be determined using  $^1\text{H}$ -MRS. In humans, it has been demonstrated that total myocardial Cr levels are decreased in dilated cardiomyopathy (82,84,85), hypertrophic cardiomyopathy (82,84,85), ischemic heart disease (82) and chronic heart failure (86). Furthermore, it was found in diseased hearts that lowered total myocardial Cr levels correlate with left ventricular ejection fraction (85) (see Table 1).

### Cr: results from animal studies

In a mouse model overexpressing myocardial Cr transporter, it was shown that a two-fold elevation in myocardial total Cr level can lead to the development of progressive hypertrophy and heart failure (112). A concentration of myocardial Cr levels of approximately 100% above normal values in mice overexpressing myocardial Cr transporter was shown to protect the heart against ischemia/reperfusion injury and myocardial stunning, but did not improve left ventricular function in the failing heart (113). In the same mouse model, it was shown that increased Cr levels together with ribose supplementation, which increases the sum of ATP, ADP and AMP concentrations, did not improve post-infarction left ventricular remodeling and function (209).

### Dixon MRI: TGs

Chemical shift-encoded fat–water separation with Dixon MRI has been increasingly applied during the last few years. Examples of cardiac Dixon MR images are given in Fig. 6. Dixon MRI provides spatial information about fat distribution and, in terms of time

efficiency, is favorable compared with  $^1\text{H}$ -MRS. Cardiac two-point Dixon imaging can be performed in approximately 15 s, whereas localized proton spectroscopy typically lasts 15–20 min (210). It has been shown that the mean myocardial fat fraction, as assessed in healthy volunteers using two-point Dixon MRI, is  $1.04 \pm 0.4\%$  of the water signal. It also displays a strong correlation ( $r = 0.79$ ;  $p < 0.05$ ) with the fat fractions assessed using  $^1\text{H}$ -MRS (210). However, in the same study, it was shown that Dixon MRI overestimated the fat fraction in the case of low cardiac lipid content. Fat–water-separated imaging can be used for the detection of intramyocardial fat (210), fibrofatty infiltration (20) and improved visualization of the pericardium as a dark structure between bright layers of fat (211). In the original MR sequence proposed by Dixon, two separate images are acquired with a spin-echo pulse sequence. One image contains the water and fat signals in phase and the other image contains the water and fat signals with opposite phase. Using subtraction and addition of the two images, water-only and fat-only images can be generated (212). To achieve fat–water separation, the choice of TEs is usually restricted. In the presence of  $B_0$  field inhomogeneity, this method is sensitive to errors. In addition, using the two-point Dixon method, it is difficult to distinguish whether the water or fat fraction is dominant and to correct for  $T_2^*$  relaxation. Therefore, various modifications to the two-point Dixon technique have been proposed, including three-point Dixon (213), modified Dixon (mDIXON) (214,215), iterative decomposition of water and fat with echo asymmetry and least-squares estimation (IDEAL) (216) and variable projection (VARPRO) (217). The Dixon techniques have been extensively reviewed elsewhere (218).

Kellman *et al.* (20) demonstrated that multi-echo Dixon imaging with fat and water separation using the VARPRO multipoint Dixon reconstruction method is a sensitive means of detecting intramyocardial fat. In addition, the three-point Dixon technique also enables the detection of myocardial fat deposition in patients with chronic myocardial infarction (219). It would be highly valuable to compare myocardial lipid quantification with these improved Dixon techniques with MRS using *ex vivo* lipid quantification as a reference standard.

### Hyperpolarized $^{13}\text{C}$ -MRS

Metabolic fluxes can be measured with MTS and by using the infusion of isotope-enriched substrates.  $^{13}\text{C}$  spectroscopy can be used to study cardiac substrate preference and metabolic activity, thereby adding valuable information about metabolic fluxes in the heart. The natural abundance of  $^{13}\text{C}$  nuclei is around 1.1%. When administering  $^{13}\text{C}$ -enriched metabolites, the signal will increase. The selective enrichment of substrates makes it possible to follow metabolic pathways in real time. An emerging technique to investigate specific metabolic pathways with increased sensitivity is the hyperpolarization technique, which can be used to enhance nuclear polarization. The polarization reflects the population difference between spin states. Different techniques can be applied, whereby the signal from a sample for use *in vivo* temporarily can be increased by 10 000-fold or more compared with equilibrium conditions, as reviewed previously (220). For *in vivo* cardiac applications, mainly dynamic nuclear polarization (DNP) is used. The DNP technique has been described in detail by Ardenkjaer-Larsen *et al.* (221). Briefly, to obtain hyperpolarization using the DNP technique, a  $^{13}\text{C}$ -containing molecule is mixed with an electron paramagnetic agent. The mixed sample is positioned in a magnetic field and rapidly cooled

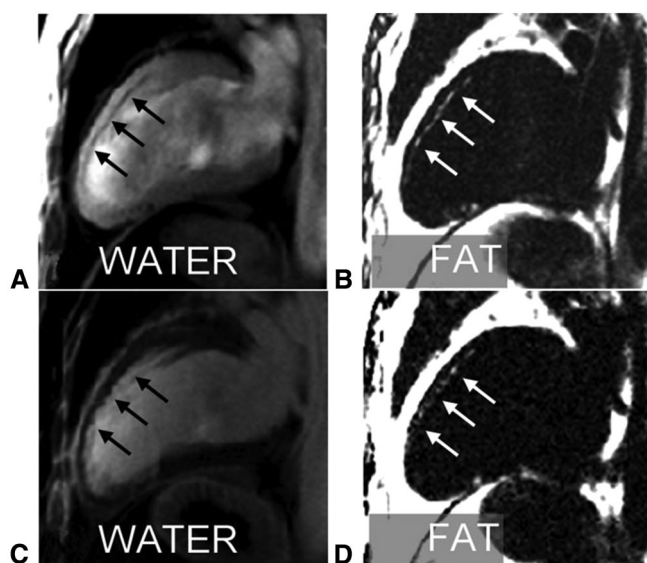


**Figure 6.** Water- and fat-separated images using the multi-echo Dixon method for a patient with chronic myocardial infarction showing fatty infiltration: (A, B) precontrast; (C, D) phase-sensitive inversion recovery late enhancement. Reproduced from ref. (20) [Kellman P, Hernando D, Shah S, Zuehlsdorff S, Jerecic R, Mancini C, Liang ZP, Arai AE. Multiecho Dixon fat and water separation method for detecting fibrofatty infiltration in the myocardium. *Magn. Reson. Med.* 2008; 61: 215–221. Copyright (c) 2008 Wiley-Liss, Inc.].

in liquid helium. By reducing the sample temperature, the free electrons become almost 100% polarized. The electron polarization is transferred to the  $^{13}\text{C}$  nucleus by microwave irradiation. The process takes between 30 and 60 min, depending on the molecule to be polarized (19). To obtain hyperpolarization of a sample, only molecules with specific properties can be used, as reviewed extensively elsewhere (222). For *in vivo* applications, only nontoxic hyperpolarized molecules can be used that are taken up by the tissue of interest and metabolized very rapidly. After generating the hyperpolarized sample using DNP, the sample is rapidly melted and, subsequently, can be injected or infused. After administration of the hyperpolarized sample, the sample is metabolized and the  $^{13}\text{C}$  label is transferred to other metabolites, which can be monitored. Different hyperpolarized samples can be applied, with hyperpolarized pyruvate being most commonly used. An example of a cardiac spectrum acquired after the infusion of  $[1\text{-}^{13}\text{C}]\text{pyruvate}$  is shown in Fig. 7. The signal strength of the hyperpolarized sample is linearly dependent on the concentration and polarization of the sample. Therefore, often, supraphysiological concentrations of the hyperpolarized substrates are used. Schroeder *et al.* (223) introduced a protocol to optimize the hyperpolarized metabolic tracer concentrations to ensure adequate MR signal with minimum metabolic perturbation. As a result of the rapid loss of signal enhancement, data must be acquired as fast as possible after administration of the hyperpolarized sample. Therefore, it is essential that the equipment needed for polarization is situated close to the MR system. In addition, one must be aware of the unrecoverable loss of the hyperpolarized spin states as a result of  $T_1$  relaxation (224), typically in a time span of 1–2 min (225). For cardiac hyperpolarized  $^{13}\text{C}$ -MRS, cardiac-gated pulse acquire experiments can be performed (226,227). A disadvantage of performing a pulse-acquire experiment is that signals are 'localized' to the sensitive volume of the surface coil. It has also been demonstrated that CSI can be used for localized cardiac hyperpolarized  $^{13}\text{C}$ -MRI (228). In this study, an elliptical central  $k$ -space sampling order scheme is applied that is less sensitive to motion, and the number of phase-encoding steps is reduced to reduce the scan time. Later, a spiral pulse sequence for rapid multislice imaging of cardiac hyperpolarized metabolic products was developed, permitting whole-heart coverage in any plane (229). More recently, Bloch–Siegert  $B_1$  mapping was integrated into the multislice cardiac-gated spiral pulse sequence to improve quantitative measurements of hyperpolarized  $^{13}\text{C}$  metabolism (230).

Most cardiac *in vivo* experiments are performed using a form of  $[^{13}\text{C}]\text{pyruvate}$  to monitor cardiac oxidative metabolism (128).

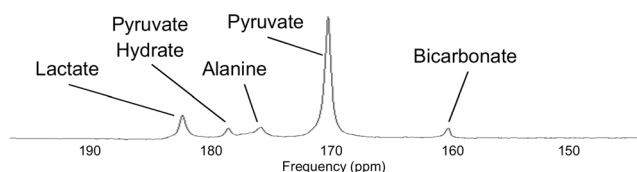


**Figure 7.** *In vivo* spectrum from the heart of a male Wistar rat obtained 10 s after injection of hyperpolarized  $[1\text{-}^{13}\text{C}]\text{pyruvate}$ . Resonances from injected pyruvate (and its equilibrium product pyruvate hydrate) and the metabolic products lactate, alanine and bicarbonate are indicated. Reproduced from ref. (128) [Schroeder MA, Cochlin LE, Heather LC, Clarke K, Radda GK, Tyler DJ. *In vivo* assessment of pyruvate dehydrogenase flux in the heart using hyperpolarized carbon-13 magnetic resonance. *Proc. Natl. Acad. Sci. U S A*, 2008; 105: 12 051–12 056. Copyright (2008) National Academy of Sciences, U.S.A.].

The metabolic products of **hyperpolarized  $[1\text{-}^{13}\text{C}]\text{pyruvate}$**  are  $[1\text{-}^{13}\text{C}]\text{lactate}$ ,  $[1\text{-}^{13}\text{C}]\text{alanine}$  and  $^{13}\text{CO}_2$ . The conversion of pyruvate to lactate, alanine or  $^{13}\text{CO}_2$  is catalyzed by the enzymes lactate dehydrogenase (LDH), alanine transaminase (AAT) and PDH, respectively (Fig. 1, green arrows indicate the detectable metabolites from  $[1\text{-}^{13}\text{C}]\text{pyruvate}$ ).  $\text{H}^{13}\text{CO}_3^-$  is in equilibrium with  $^{13}\text{CO}_2$  under the action of the carbonic anhydrase enzyme. It has been suggested that the mitochondrial conversion of pyruvate to  $\text{H}^{13}\text{CO}_3^-$  can be used as a marker for the activity of the PDH complex *in vivo* (231). Indeed, it was shown that the hyperpolarized MRS measurements of PDH flux correlated significantly with *ex vivo* measurements of PDH enzyme activity (232). Decreased myocardial PDH flux was observed in a rat model of type 1 diabetes *in vivo*, pointing to an almost exclusive use of fatty acids and ketone bodies for energy requirements (128). A higher PDH activity was observed in fasted long-chain acyl-CoA dehydrogenase knockout mice compared with wild-type mice, because of the elevated reliance on glucose oxidation in these mice during fasting (124). PDH activity is partially controlled by pyruvate dehydrogenase kinase (PDK), the activity of which is, in turn, affected by high acetyl-CoA/CoA and NADH/NAD $^+$  ratios. During fasting, fatty acids are converted to acetyl-CoA formed by mitochondrial  $\beta$ -oxidation, resulting in an up-regulation of PDK activity and a down-regulation of PDH activity. Injection of glucose, insulin and potassium in fasted rats leads to an increased flux of pyruvate through the PDH complex (233). In fed rats with high PDH activity, pyruvate oxidation is limited by feedback inhibition from acetyl-CoA (234).

In healthy pig hearts, it has been shown that the conversion rate of hyperpolarized  $[1\text{-}^{13}\text{C}]\text{pyruvate}$  is increased by inotropic stress induced during dobutamine infusion compared with the resting condition (235).

As demonstrated in isolated as well as *in vivo* rat heart, hyperpolarized  $[1\text{-}^{13}\text{C}]\text{pyruvate}$  can be administered to measure intracellular pH (236). To calculate pH, signals from both  $\text{H}^{13}\text{CO}_3^-$  and  $^{13}\text{CO}_2$  are required. A drawback is that the  $^{13}\text{CO}_2$  signal is relatively weak.

After the infusion of **hyperpolarized  $[2\text{-}^{13}\text{C}]\text{pyruvate}$** , the conversion to  $[2\text{-}^{13}\text{C}]\text{lactate}$ ,  $[1\text{-}^{13}\text{C}]\text{acetylcarnitine}$  and  $[1\text{-}^{13}\text{C}]\text{citrate}$  can be followed, together with the TCA cycle-mediated conversion into  $[5\text{-}^{13}\text{C}]\text{glutamate}$  in the rat heart *in vivo* (237). The conversion of  $[2\text{-}^{13}\text{C}]\text{pyruvate}$  to  $[2\text{-}^{13}\text{C}]\text{lactate}$  provides information about glycolysis, whereas the conversion to  $[1\text{-}^{13}\text{C}]\text{acetylcarnitine}$  provides information about the PDH flux (238). Acetylcarnitine is produced by mitochondrial carnitine acetyltransferase, stimulated by acetyl-CoA and carnitine (Fig. 1, orange arrows indicate the detectable metabolites from  $[2\text{-}^{13}\text{C}]\text{pyruvate}$ ). It has been shown that acetylcarnitine acts to fine-tune the acetyl-CoA availability in the rat heart (237).

Using dual-labeled **hyperpolarized  $[1,2\text{-}^{13}\text{C}_2]\text{pyruvate}$** , combined with an interleaved acquisition scheme with selective excitation for  $^{13}\text{CO}_2$ , it is possible to observe metabolites resulting from the PDH and TCA cycle flux, as well as to determine the pH (239) (see also Fig. 1, in which the purple arrows indicate the detectable metabolites from  $[1,2\text{-}^{13}\text{C}_2]\text{pyruvate}$ ). A limitation of using dual-labeled hyperpolarized  $[1,2\text{-}^{13}\text{C}_2]\text{pyruvate}$  at field strengths of  $\leq 3\text{ T}$  are the overlapping resonances of  $[5\text{-}^{13}\text{C}]\text{glutamate}$  with  $[1\text{-}^{13}\text{C}]\text{lactate}$  and  $[1\text{-}^{13}\text{C}]\text{acetylcarnitine}$  with  $[1\text{-}^{13}\text{C}]\text{pyruvate}$ . However, because both  $[1\text{-}^{13}\text{C}]\text{lactate}$  and  $[1\text{-}^{13}\text{C}]\text{pyruvate}$  give doublet resonances, the area of the overlapping peaks can be compensated for when no other overlap occurs. As shown in pigs, an advantage of using dual-labeled hyperpolarized  $[1,2\text{-}^{13}\text{C}_2]\text{pyruvate}$  is the lower dose required to obtain the same SNR (239).

Using a combination of both  $[1-^{13}\text{C}]$ pyruvate and  $[2-^{13}\text{C}]$ pyruvate, the relationship between pyruvate dehydrogenase complex (PDC)-mediated oxidation of pyruvate and its subsequent incorporation into the TCA cycle can be followed (240). It was shown that a significant PDK-mediated reduction in PDH flux, which, in turn, diminishes the contribution of glucose oxidation to energy generation, contributes to the pathology of the hyperthyroid rat heart *in vivo* (129). In spontaneous hypertensive rat hearts, a preference for glucose metabolism was observed, as an increase in PDH flux was found (131). In rats with surgically induced myocardial infarction, a decrease in TCA cycle activity was observed, which correlated with the degree of cardiac dysfunction 6 weeks after myocardial infarction. The decrease in TCA cycle activity was independent of alterations in PDH flux (132). In pigs, it was shown that pyruvate metabolism changes throughout the development of dilated cardiomyopathy and that reduced pyruvate oxidation by PDC reveals the onset of overt heart failure (130).

In addition to pyruvate, lactate is also an important energy source for the heart (2). The observable metabolic products of hyperpolarized  $[1-^{13}\text{C}]$ lactate were shown to be  $^{13}\text{C}$ -pyruvate,  $^{13}\text{C}$ -alanine and  $^{13}\text{C}$ -bicarbonate (241). It has been demonstrated recently that hyperpolarized  $[1-^{13}\text{C}]$ lactate can also be used to measure cardiac metabolism in rat hearts *in vivo* (242), thereby providing information about the PDH flux (Fig. 1, pink arrows indicate the detectable metabolites from  $[1-^{13}\text{C}]$ lactate). As the physiological plasma concentrations of lactate can be higher than those of pyruvate [1–10 mM (242) versus 3–6 mM (243), respectively], the use of lactate may represent a viable and potentially safer alternative to pyruvate, as higher concentrations of lactate can be used to achieve an increase in SNR. Recently, it was shown that neat  $[1-^{13}\text{C}]$ lactic acid without the addition of any solvent or glassing agent can be used for the preparation of hyperpolarized  $[1-^{13}\text{C}]$ lactate in solution (244).

Furthermore, the feasibility of using hyperpolarized  $[1-^{13}\text{C}]$ butyrate to provide information on the metabolism of short-chain fatty acid and ketone bodies has recently been demonstrated in isolated and *in vivo* rat hearts (245). After infusion, the hyperpolarized  $[1-^{13}\text{C}]$ butyrate is transported into the cell via the monocarboxylate transporter enzyme, where it is metabolized to  $\beta$ -hydroxybutyryl-CoA and acetoacetyl-CoA before conversion into ketone bodies (acetoacetate and  $\beta$ -hydroxybutyrate) and acetyl-CoA (which enters the TCA cycle). In Fig. 1, some detectable metabolites from  $[1-^{13}\text{C}]$ butyrate are indicated with brown arrows.

Until now, cardiac hyperpolarized  $^{13}\text{C}$  imaging and spectroscopy have only been applied in animals *in vivo*. However, the first study in which hyperpolarized  $[1-^{13}\text{C}]$ pyruvate was used in patients with prostate cancer has been published recently (246). This study shows that hyperpolarized  $[1-^{13}\text{C}]$ pyruvate can safely be used in humans *in vivo* with the potential for promising results for noninvasive cancer diagnosis and treatment monitoring in future clinical trials. Therefore, this study paves the way for other clinical trials in which cardiac diseases can be studied.

### Clinical Translation

In contrast with cardiac MRI, cardiac metabolic MRS must overcome several methodological challenges before it can be broadly applied clinically. These challenges include minimization of the scan time and an increase in SNR. The scan time in MRS is relatively long because of the low metabolite concentrations,

which require numerous signal averages to obtain sufficient SNR. Advanced shimming algorithms, the use of hyperpolarized nuclei and/or scanning at a higher magnetic field strength can improve SNR. The ongoing development of multichannel detection coils, RF pulses and pulse sequences will further improve cardiac MRS, thereby increasing its usability for clinical applications. In addition, faster implementation of promising research applications on clinical scanners by the vendors is a prerequisite to make the broad application of these techniques possible. Finally, further development of more automated algorithms for spectral analysis and quantification may contribute to the routine clinical application of cardiac MRS.

## Acknowledgements

This work was performed within the framework of CTMM, the Centre for Translational Molecular Medicine, project PREDICt (grant number 01C-104), and was supported by the Dutch Heart Foundation, Dutch Diabetes Research Foundation and Dutch Kidney Foundation.

V. B. Schrauwen-Hinderling is supported by a VENI (grant 91611136) for innovative research from the Netherlands Organization for Scientific Research (NWO). M. E. Kooi is supported by an NWO Aspasia grant (015.008.047).

## REFERENCES

- Onay-Besikci A. Regulation of cardiac energy metabolism in newborn. *Mol. Cell. Biochem.* 2006; 287: 1–11.
- Taegtmeyer H. Energy metabolism of the heart: from basic concepts to clinical applications. *Curr. Probl. Cardiol.* 1994; 19: 59–113.
- Lopaschuk GD, Belke DD, Gamble J, Itoi T, Schonekess BO. Regulation of fatty acid oxidation in the mammalian heart in health and disease. *Biochim. Biophys. Acta*, 1994; 1213: 263–276.
- Stanley WC, Lopaschuk GD, Hall JL, McCormack JG. Regulation of myocardial carbohydrate metabolism under normal and ischaemic conditions. Potential for pharmacological interventions. *Cardiovasc. Res.* 1997; 33: 243–257.
- Taha M, Lopaschuk GD. Alterations in energy metabolism in cardiomyopathies. *Ann. Med.* 2007; 39: 594–607.
- Kenchaiah S, Evans JC, Levy D, Wilson PW, Benjamin EJ, Larson MG, Kannel WB, Vasan RS. Obesity and the risk of heart failure. *N. Engl. J. Med.* 2002; 347: 305–313.
- Nichols GA, Gullion CM, Koro CE, Ephross SA, Brown JB. The incidence of congestive heart failure in type 2 diabetes: an update. *Diabetes Care*, 2004; 27: 1879–1884.
- Taegtmeyer H, McNulty P, Young ME. Adaptation and maladaptation of the heart in diabetes: part I: general concepts. *Circulation*, 2002; 105: 1727–1733.
- Young ME, McNulty P, Taegtmeyer H. Adaptation and maladaptation of the heart in diabetes: part II: potential mechanisms. *Circulation*, 2002; 105: 1861–1870.
- Harnancey R, Wilson CR, Taegtmeyer H. Adaptation and maladaptation of the heart in obesity. *Hypertension*, 2008; 52: 181–187.
- Zhou YT, Grayburn P, Karim A, Shimabukuro M, Higa M, Baetens D, Orci L, Unger RH. Lipotoxic heart disease in obese rats: implications for human obesity. *Proc. Natl. Acad. Sci. U S A*, 2000; 97: 1784–1789.
- Wende AR, Abel ED. Lipotoxicity in the heart. *Biochim. Biophys. Acta*, 2010; 1801: 311–319.
- Kim RJ, Fieno DS, Parrish TB, Harris K, Chen EL, Simonetti O, Bundy J, Finn JP, Klocke FJ, Judd RM. Relationship of MRI delayed contrast enhancement to irreversible injury, infarct age, and contractile function. *Circulation*, 1999; 100: 1992–2002.
- Parsai C, O'Hanlon R, Prasad SK, Mohiaddin RH. Diagnostic and prognostic value of cardiovascular magnetic resonance in non-ischaemic cardiomyopathies. *J. Cardiovasc. Magn. Reson.* 2012; 14: 54.
- Bottomley PA (ed.). *NMR Spectroscopy of the Human Heart*. John Wiley: Chichester; 2009.
- Bottomley PA, Panjath GS, Lai S, Hirsch GA, Wu K, Najjar SS, Steinberg A, Gerstenblith G, Weiss RG. Metabolic rates of ATP



- transfer through creatine kinase (CK Flux) predict clinical heart failure events and death. *Sci. Transl. Med.* 2013; 5: 215re213.
17. Neubauer S, Horn M, Cramer M, Harre K, Newell JB, Peters W, Pabst T, Ertl G, Hahn D, Ingwall JS, Kochsiek K. Myocardial phosphocreatine-to-ATP ratio is a predictor of mortality in patients with dilated cardiomyopathy. *Circulation*, 1997; 96: 2190–2196.
18. Szczepaniak LS, Dobbins RL, Metzger GJ, Sartoni-D'Ambrosia G, Arbique D, Vongpatanasin W, Unger R, Victor RG. Myocardial triglycerides and systolic function in humans: in vivo evaluation by localized proton spectroscopy and cardiac imaging. *Magn. Reson. Med.* 2003; 49: 417–423.
19. Schroeder MA, Clarke K, Neubauer S, Tyler DJ. Hyperpolarized magnetic resonance: a novel technique for the in vivo assessment of cardiovascular disease. *Circulation*, 2011; 124: 1580–1594.
20. Kellman P, Hernando D, Shah S, Zuehlsdorff S, Jerecic R, Mancini C, Liang ZP, Arai AE. Multiecho Dixon fat and water separation method for detecting fibrofatty infiltration in the myocardium. *Magn. Reson. Med.* 2009; 61: 215–221.
21. Bottomley PA. Noninvasive study of high-energy phosphate metabolism in human heart by depth-resolved  $^{31}\text{P}$  NMR spectroscopy. *Science*, 1985; 229: 769–772.
22. Tyler DJ, Hudsmith LE, Clarke K, Neubauer S, Robson MD. A comparison of cardiac ( $^{31}\text{P}$ ) MRS at 1.5 and 3 T. *NMR Biomed.* 2008; 21: 793–798.
23. Rodgers CT, Clarke WT, Snyder C, Vaughan JT, Neubauer S, Robson MD. Human cardiac ( $^{31}\text{P}$ ) magnetic resonance spectroscopy at 7 tesla. *Magn. Reson. Med.* 2014; 72: 304–315.
24. Schneider JE, Cassidy PJ, Lygate C, Tyler DJ, Wiesmann F, Grieve SM, Hulbert K, Clarke K, Neubauer S. Fast, high-resolution in vivo cine magnetic resonance imaging in normal and failing mouse hearts on a vertical 11.7 T system. *J. Magn. Reson. Imaging*, 2003; 18: 691–701.
25. Gutberlet M, Noeske R, Schwinge K, Freyhardt P, Felix R, Niendorf T. Comprehensive cardiac magnetic resonance imaging at 3.0 Tesla: feasibility and implications for clinical applications. *Invest. Radiol.* 2006; 41: 154–167.
26. Oz G, Tkac I, Ugurbil K. Animal models and high field imaging and spectroscopy. *Dialogues Clin. Neurosci.* 2013; 15: 263–278.
27. Atalay MK, Poncelet BP, Kantor HL, Brady TJ, Weisskoff RM. Cardiac susceptibility artifacts arising from the heart–lung interface. *Magn. Reson. Med.* 2001; 45: 341–345.
28. Venkatesh BA, Lima JA, Bluemke DA, Lai S, Steenbergen C, Liu CY. MR proton spectroscopy for myocardial lipid deposition quantification: a quantitative comparison between 1.5 T and 3 T. *J. Magn. Reson. Imaging*, 2012; 36: 1222–1230.
29. Schneider JE, Tyler DJ, ten Hove M, Sang AE, Cassidy PJ, Fischer A, Wallis J, Sebag-Montefiore LM, Watkins H, Isbrandt D, Clarke K, Neubauer S. In vivo cardiac  $^1\text{H}$ -MRS in the mouse. *Magn. Reson. Med.* 2004; 52: 1029–1035.
30. Bakermans AJ, Geraedts TR, van Weeghel M, Denis S, Joao Ferraz M, Aerts JM, Aten J, Nicolay K, Houten SM, Prompers JJ. Fasting-induced myocardial lipid accumulation in long-chain acyl-CoA dehydrogenase knockout mice is accompanied by impaired left ventricular function. *Circ. Cardiovasc. Imaging*, 2011; 4: 558–565.
31. Tucci S, Flögel U, Hermann S, Sturm M, Schafers M, Spiekerkoetter U. Development and pathomechanisms of cardiomyopathy in very long-chain acyl-CoA dehydrogenase deficient (VLCAD(–/–)) mice. *Biochim. Biophys. Acta*, 2014; 1842: 677–685.
32. Gruetter R. Automatic, localized in vivo adjustment of all first- and second-order shim coils. *Magn. Reson. Med.* 1993; 29: 804–811.
33. Gruetter R, Boesch C. Fast, noninteractive shimming of spatially localized signals. *J. Magn. Reson.* 1992; 96: 323–334.
34. Jaffer FA, Wen H, Balaban RS, Wolff SD. A method to improve the B0 homogeneity of the heart in vivo. *Magn. Reson. Med.* 1996; 36: 375–383.
35. Schär M, Kozerke S, Harvey PA, Boesiger P. Local linear shimming for cardiac SSFP imaging at 3 T. *Proc. Int. Soc. Magn. Reson. Med.* 2002; 2002.
36. Kubach MR, Bornstedt A, Hombach V, Merkle N, Schar M, Spiess J, Nienhaus GU, Rasche V. Cardiac phase-specific shimming (CPSS) for SSFP MR cine imaging at 3 T. *Phys. Med. Biol.* 2009; 54: N467–N478.
37. Shah S, Kellman P, Greiser A, Weale PJ, Zuehlsdorff S, Jerecic R. Rapid fieldmap estimation for cardiac shimming. *Proc. Int. Soc. Magn. Reson. Med.* 2009; 2009.
38. Schär M, Vonken EJ, Stuber M. Simultaneous B(0)- and B(1) + -map acquisition for fast localized shim, frequency, and RF power determination in the heart at 3 T. *Magn. Reson. Med.* 2010; 63: 419–426.
39. Cunningham CH, Pauly JM, Nayak KS. Saturated double-angle method for rapid B1+ mapping. *Magn. Reson. Med.* 2006; 55: 1326–1333.
40. Giovannetti G, Hartwig V, Frijia F, Menichetti L, Positano V, Ardenkjaer-Larsen JH, Lionetti V, Donato Aquaro G, De Marchi D, Flori A, Landini L, Lombardi M, Santarelli MF. Hyperpolarized  $^{13}\text{C}$  MRS cardiac metabolism studies in pigs: comparison between surface and volume radiofrequency coils. *Appl. Magn. Reson.* 2012; 42: 413–428.
41. Bottomley PA, Lugo Olivieri CH, Giaquinto R. What is the optimum phased array coil design for cardiac and torso magnetic resonance? *Magn. Reson. Med.* 1997; 37: 591–599.
42. Wright SM, Wald LL. Theory and application of array coils in MR spectroscopy. *NMR Biomed.* 1997; 10: 394–410.
43. Weiss K, Martini N, Boesiger P, Kozerke S. Cardiac proton spectroscopy using large coil arrays. *NMR Biomed.* 2013; 26: 276–284.
44. Sandgren N, Stoica P, Frigo FJ, Selen Y. Spectral analysis of multi-channel MRS data. *J. Magn. Reson.* 2005; 175: 79–91.
45. Brown MA. Time-domain combination of MR spectroscopy data acquired using phased-array coils. *Magn. Reson. Med.* 2004; 52: 1207–1213.
46. Maril N, Lenkinski RE. An automated algorithm for combining multivoxel MRS data acquired with phased-array coils. *J. Magn. Reson. Imaging*, 2005; 21: 317–322.
47. Rodgers CT, Robson MD. Receive array magnetic resonance spectroscopy: whitened singular value decomposition (WSVD) gives optimal Bayesian solution. *Magn. Reson. Med.* 2010; 63: 881–891.
48. Barany M, Langer BG, Glick RP, Venkatasubramanian PN, Wilbur AC, Spigos DG. In vivo  $^1\text{H}$ -1 spectroscopy in humans at 1.5 T. *Radiology*, 1988; 167: 839–844.
49. Lanzer P, Barta C, Botvinick EH, Wiesendanger HU, Modin G, Higgins CB. ECG-synchronized cardiac MR imaging: method and evaluation. *Radiology*, 1985; 155: 681–686.
50. Felblinger J, Jung B, Slotboom J, Boesch C, Kreis R. Methods and reproducibility of cardiac/respiratory double-triggered ( $^1\text{H}$ )-MR spectroscopy of the human heart. *Magn. Reson. Med.* 1999; 42: 903–910.
51. van der Meer RW, Doornbos J, Kozerke S, Schar M, Bax JJ, Hammer S, Smit JW, Romijn JA, Diamant M, Rijzewijk LJ, de Roos A, Lamb HJ. Metabolic imaging of myocardial triglyceride content: reproducibility of  $^1\text{H}$  MR spectroscopy with respiratory navigator gating in volunteers. *Radiology*, 2007; 245: 251–257.
52. Kankaanpää M, Lehto HR, Parkka JP, Komu M, Viljanen A, Ferrannini E, Knuuti J, Nuutila P, Parkkola R, Iozzo P. Myocardial triglyceride content and epicardial fat mass in human obesity: relationship to left ventricular function and serum free fatty acid levels. *J. Clin. Endocrinol. Metab.* 2006; 91: 4689–4695.
53. Felblinger J, Boesch C. Amplitude demodulation of the electrocardiogram signal (ECG) for respiration monitoring and compensation during MR examinations. *Magn. Reson. Med.* 1997; 38: 129–136.
54. Schar M, Kozerke S, Boesiger P. Navigator gating and volume tracking for double-triggered cardiac proton spectroscopy at 3 Tesla. *Magn. Reson. Med.* 2004; 51: 1091–1095.
55. Rial B, Robson MD, Neubauer S, Schneider JE. Rapid quantification of myocardial lipid content in humans using single breath-hold  $^1\text{H}$  MRS at 3 Tesla. *Magn. Reson. Med.* 2011; 66: 619–624.
56. Santelli C, Nezafat R, Goddu B, Manning WJ, Smink J, Kozerke S, Peters DC. Respiratory bellows revisited for motion compensation: preliminary experience for cardiovascular MR. *Magn. Reson. Med.* 2011; 65: 1097–1102.
57. Kozerke S, Schar M, Lamb HJ, Boesiger P. Volume tracking cardiac  $^{31}\text{P}$  spectroscopy. *Magn. Reson. Med.* 2002; 48: 380–384.
58. Wilson SJ, Brereton IM, Hockings P, Roffmann W, Doddrell DM. Respiratory triggered imaging with an optical displacement sensor. *Magn. Reson. Imaging*, 1993; 11: 1027–1032.
59. Burdett NG, Carpenter TA, Hall LD. A simple device for respiratory gating for the MRI of laboratory animals. *Magn. Reson. Imaging*, 1993; 11: 897–901.
60. Lemieux SK, Glover GH. An infrared device for monitoring the respiration of small rodents during magnetic resonance imaging. *J. Magn. Reson. Imaging*, 1996; 6: 561–564.
61. Minard KR, Wind RA, Phelps RL. A compact respiratory-triggering device for routine microimaging of laboratory mice. *J. Magn. Reson. Imaging*, 1998; 8: 1343–1348.



62. Fishbein KW, McConville P, Spencer RG. The lever-coil: a simple, inexpensive sensor for respiratory and cardiac motion in MRI experiments. *Magn. Reson. Imaging*, 2001; 19: 881–889.
63. Wiesmann F, Szimtenings M, Frydrychowicz A, Illinger R, Hunecke A, Rommel E, Neubauer S, Haase A. High-resolution MRI with cardiac and respiratory gating allows for accurate in vivo atherosclerotic plaque visualization in the murine aortic arch. *Magn. Reson. Med.* 2003; 50: 69–74.
64. Sablong R, Rengle A, Ramgolan A, Saint-Jalmes H, Beuf O. An optical fiber-based gating device for prospective mouse cardiac MRI. *IEEE Trans. Biomed. Eng.* 2014; 61: 162–170.
65. Cassidy PJ, Schneider JE, Grieve SM, Lygate C, Neubauer S, Clarke K. Assessment of motion gating strategies for mouse magnetic resonance at high magnetic fields. *J. Magn. Reson. Imaging*, 2004; 19: 229–237.
66. Provencher SW. Estimation of metabolite concentrations from localized in vivo proton NMR spectra. *Magn. Reson. Med.* 1993; 30: 672–679.
67. Naressi A, Couturier C, Castang I, de Beer R, Graveron-Demilly D. Java-based graphical user interface for MRUI, a software package for quantitation of in vivo/medical magnetic resonance spectroscopy signals. *Comput. Biol. Med.* 2001; 31: 269–286.
68. Poulet JB, Sima DM, Van Huffel S. MRS signal quantitation: a review of time- and frequency-domain methods. *J. Magn. Reson.* 2008; 195: 134–144.
69. Jansen JFA, Backes WH, Nicolay K, Kooi ME.  $^1\text{H}$  MR spectroscopy of the brain: absolute quantification of metabolites. *Radiology*, 2006; 240: 318–332.
70. Meininger M, Landschütz W, Beer M, Seyfarth T, Horn M, Pabst T, Haase A, Hahn D, Neubauer S, von Kienlin M. Concentrations of human cardiac phosphorus metabolites determined by SLOOP  $^{31}\text{P}$  NMR spectroscopy. *Magn. Reson. Med.* 1999; 41: 657–663.
71. Yabe T, Mitsunami K, Inubushi T, Kinoshita M. Quantitative measurements of cardiac phosphorus metabolites in coronary artery disease by  $^{31}\text{P}$  magnetic resonance spectroscopy. *Circulation*, 1995; 92: 15–23.
72. Beer M, Seyfarth T, Sandstede J, Landschutz W, Lipke C, Kostler H, von Kienlin M, Harre K, Hahn D, Neubauer S. Absolute concentrations of high-energy phosphate metabolites in normal, hypertrophied, and failing human myocardium measured noninvasively with (31P)-SLOOP magnetic resonance spectroscopy. *J. Am. Coll. Cardiol.* 2002; 40: 1267–1274.
73. Bottomley PA. MR spectroscopy of the human heart: the status and the challenges. *Radiology*, 1994; 191: 593–612.
74. Bottomley PA, Atalar E, Weiss RG. Human cardiac high-energy phosphate metabolite concentrations by 1D-resolved NMR spectroscopy. *Magn. Reson. Med.* 1996; 35: 664–670.
75. Hoffenberg EF, Kozlowski P, Salerno TA, Deslauriers R. Evaluation of cardiac  $^{31}\text{P}$  magnetic resonance spectroscopy: reviewing NMR principles. *J. Surg. Res.* 1996; 62: 135–143.
76. Hardy CJ, Weiss RG, Bottomley PA, Gerstenblith G. Altered myocardial high-energy phosphate metabolites in patients with dilated cardiomyopathy. *Am. Heart J.* 1991; 122: 795–801.
77. Neubauer S, Krahe T, Schindler R, Horn M, Hillenbrand H, Entzeroth C, Mader H, Kromer EP, Riegger GA, Lackner K, Ertl G.  $^{31}\text{P}$  magnetic resonance spectroscopy in dilated cardiomyopathy and coronary artery disease. Altered cardiac high-energy phosphate metabolism in heart failure. *Circulation*, 1992; 86: 1810–1818.
78. Bottomley PA, Hardy CJ, Weiss RG. Correcting human heart  $^{31}\text{P}$  NMR spectra for partial saturation. Evidence that saturation factors for PCr/ATP are homogeneous in normal and disease states. *J. Magn. Reson.* 1991; 95: 341–355.
79. van der Meer RW, Rijzewijk LJ, Diamant M, Hammer S, Schar M, Bax JJ, Smit JW, Romijn JA, de Roos A, Lamb HJ. The ageing male heart: myocardial triglyceride content as independent predictor of diastolic function. *Eur. Heart J.* 2008; 29: 1516–1522.
80. McGavock JM, Lingvay I, Zib I, Tillery T, Salas N, Unger R, Levine BD, Raskin P, Victor RG, Szczepaniak LS. Cardiac steatosis in diabetes mellitus: a  $^1\text{H}$ -magnetic resonance spectroscopy study. *Circulation*, 2007; 116: 1170–1175.
81. Rijzewijk LJ, van der Meer RW, Smit JW, Diamant M, Bax JJ, Hammer S, Romijn JA, de Roos A, Lamb HJ. Myocardial steatosis is an independent predictor of diastolic dysfunction in type 2 diabetes mellitus. *J. Am. Coll. Cardiol.* 2008; 52: 1793–1799.
82. Nakae I, Mitsunami K, Yoshino T, Omura T, Tsutamoto T, Matsumoto T, Morikawa S, Inubushi T, Horie M. Clinical features of myocardial triglyceride in different types of cardiomyopathy assessed by proton magnetic resonance spectroscopy: comparison with myocardial creatine. *J. Card. Fail.* 2010; 16: 812–822.
83. Graner M, Pentikainen MO, Nyman K, Siren R, Lundbom J, Hakkarainen A, Lauerma K, Lundbom N, Nieminen MS, Petzold M, Taskinen MR. Cardiac steatosis in patients with dilated cardiomyopathy. *Heart*, 2014; 100: 1107–1112.
84. Nakae I, Mitsunami K, Omura T, Yabe T, Tsutamoto T, Matsuo S, Takahashi M, Morikawa S, Inubushi T, Nakamura Y, Kinoshita M, Horie M. Proton magnetic resonance spectroscopy can detect creatine depletion associated with the progression of heart failure in cardiomyopathy. *J. Am. Coll. Cardiol.* 2003; 42: 1587–1593.
85. Nakae I, Mitsunami K, Matsuo S, Inubushi T, Morikawa S, Tsutamoto T, Koh T, Horie M. Myocardial creatine concentration in various nonischemic heart diseases assessed by  $^1\text{H}$  magnetic resonance spectroscopy. *Circ. J.* 2005; 69: 711–716.
86. Nakae I, Mitsunami K, Matsuo S, Matsumoto T, Morikawa S, Inubushi T, Koh T, Horie M. Assessment of myocardial creatine concentration in dysfunctional human heart by proton magnetic resonance spectroscopy. *Magn. Reson. Med. Sci.* 2004; 3: 19–25.
87. Perseghin G, De Cobelli F, Esposito A, Belloni E, Lattuada G, Canu T, Invernizzi PL, Ragogna F, La Torre A, Scifo P, Alberti G, Del Maschio A, Luzi L. Left ventricular function and energy metabolism in middle-aged men undergoing long-lasting sustained aerobic oxidative training. *Heart*, 2009; 95: 630–635.
88. Scheuermann-Freestone M, Madsen PL, Manners D, Blamire AM, Buckingham RE, Styles P, Radda GK, Neubauer S, Clarke K. Abnormal cardiac and skeletal muscle energy metabolism in patients with type 2 diabetes. *Circulation*, 2003; 107: 3040–3046.
89. Diamant M, Lamb HJ, Groeneveld Y, Endert EL, Smit JWA, Bax JJ, Romijn JA, de Roos A, Radder JK. Diastolic dysfunction is associated with altered myocardial metabolism in asymptomatic normotensive patients with well-controlled type 2 diabetes mellitus. *J. Am. Coll. Cardiol.* 2003; 42: 328–335.
90. Rijzewijk LJ, van der Meer RW, Lamb HJ, de Jong HW, Lubberink M, Romijn JA, Bax JJ, de Roos A, Twisk JW, Heine RJ, Lammertsma AA, Smit JW, Diamant M. Altered myocardial substrate metabolism and decreased diastolic function in nonischemic human diabetic cardiomyopathy: studies with cardiac positron emission tomography and magnetic resonance imaging. *J. Am. Coll. Cardiol.* 2009; 54: 1524–1532.
91. Mitsunami K, Okada M, Inoue T, Hachisuka M, Kinoshita M, Inubushi T. In vivo  $^{31}\text{P}$  nuclear magnetic resonance spectroscopy in patients with old myocardial infarction. *Jpn. Circ. J.* 1992; 56: 614–619.
92. Weiss RG, Bottomley PA, Hardy CJ, Gerstenblith G. Regional myocardial metabolism of high-energy phosphates during isometric exercise in patients with coronary artery disease. *N. Engl. J. Med.* 1990; 323: 1593–1600.
93. Beer M, Spindler M, Sandstede JJ, Remmert H, Beer S, Kostler H, Hahn D. Detection of myocardial infarctions by acquisition-weighted  $^{31}\text{P}$ -MR spectroscopy in humans. *J. Magn. Reson. Imaging*, 2004; 20: 798–802.
94. Beer M, Sandstede J, Landschutz W, Viehrieg M, Harre K, Horn M, Meininger M, Pabst T, Kenn W, Haase A, von Kienlin M, Neubauer S, Hahn D. Altered energy metabolism after myocardial infarction assessed by  $^{31}\text{P}$ -MR-spectroscopy in humans. *Eur. Radiol.* 2000; 10: 1323–1328.
95. Hansch A, Rzanny R, Heyne JP, Leder U, Reichenbach JR, Kaiser WA. Noninvasive measurements of cardiac high-energy phosphate metabolites in dilated cardiomyopathy by using  $^{31}\text{P}$  spectroscopic chemical shift imaging. *Eur. Radiol.* 2005; 15: 319–323.
96. Shivu GN, Abozguia K, Phan TT, Ahmed I, Henning A, Frenneaux M. (31P) magnetic resonance spectroscopy to measure in vivo cardiac energetics in normal myocardium and hypertrophic cardiomyopathy: experiences at 3 T. *Eur. J. Radiol.* 2010; 73: 255–259.
97. Beer M, Buchner S, Wirbelauer J, Fuchs J, Machann W, Ritter CO, Beissert M, Darge K, Hahn D, Kostler H. MR imaging and MR spectroscopy for characterization of cardiomyopathies in adolescents – preliminary results. *Rof. 2007; 179: 932–937.*
98. Crilly JG, Boehm EA, Blair E, Rajagopalan B, Blamire AM, Styles P, McKenna WJ, Ostman-Smith I, Clarke K, Watkins H. Hypertrophic cardiomyopathy due to sarcomeric gene mutations is characterized by impaired energy metabolism irrespective of the degree of hypertrophy. *J. Am. Coll. Cardiol.* 2003; 41: 1776–1782.
99. Masuda Y, Tateno Y, Ikehira H, Hashimoto T, Shishido F, Sekiya M, Imazeki Y, Imai H, Watanabe S, Inagaki Y. High-energy phosphate

- metabolism of the myocardium in normal subjects and patients with various cardiomyopathies—the study using ECG gated MR spectroscopy with a localization technique. *Jpn. Circ. J.* 1992; 56: 620–626.
100. Phan TT, Abozguia K, Nallur Shivu G, Mahadevan G, Ahmed I, Williams L, Dwivedi G, Patel K, Steendijk P, Ashrafian H, Henning A, Frenneaux M. Heart failure with preserved ejection fraction is characterized by dynamic impairment of active relaxation and contraction of the left ventricle on exercise and associated with myocardial energy deficiency. *J. Am. Coll. Cardiol.* 2009; 54: 402–409.
101. Spoladore R, Fragasso G, Perseghin G, De Cobelli F, Esposito A, Maranta F, Calori G, Locatelli M, Lattuada G, Scifo P, Del Maschio A, Margonato A. Beneficial effects of beta-blockers on left ventricular function and cellular energy reserve in patients with heart failure. *Fundam. Clin. Pharmacol.* 2013; 27: 455–464.
102. Fragasso G, Perseghin G, De Cobelli F, Esposito A, Palloschi A, Lattuada G, Scifo P, Calori G, Del Maschio A, Margonato A. Effects of metabolic modulation by trimetazidine on left ventricular function and phosphocreatine/adenosine triphosphate ratio in patients with heart failure. *Eur. Heart J.* 2006; 27: 942–948.
103. Perseghin G, Lattuada G, De Cobelli F, Esposito A, Belloni E, Ntali G, Ragogna F, Canu T, Scifo P, Del Maschio A, Luzi L. Increased mediastinal fat and impaired left ventricular energy metabolism in young men with newly found fatty liver. *Hepatology*, 2008; 47: 51–58.
104. Sieverding L, Jung WJ, Breuer J, Widmaier S, Staubert A, van Erckelen F, Schmidt O, Bunse M, Hoess T, Lutz O, Dietze GJ, Apitz J. Proton-decoupled myocardial <sup>31</sup>P NMR spectroscopy reveals decreased PCr/Pi in patients with severe hypertrophic cardiomyopathy. *Am. J. Cardiol.* 1997; 80: 34A–40A.
105. Smith CS, Bottomley PA, Schulman SP, Gerstenblith G, Weiss RG. Altered creatine kinase adenosine triphosphate kinetics in failing hypertrophied human myocardium. *Circulation*, 2006; 114: 1151–1158.
106. Abraham MR, Bottomley PA, Dimaano VL, Pinheiro A, Steinberg A, Traill TA, Abraham TP, Weiss RG. Creatine kinase adenosine triphosphate and phosphocreatine energy supply in a single kindred of patients with hypertrophic cardiomyopathy. *Am. J. Cardiol.* 2013; 112: 861–866.
107. Bottomley PA, Wu KC, Gerstenblith G, Schulman SP, Steinberg A, Weiss RG. Reduced myocardial creatine kinase flux in human myocardial infarction: an in vivo phosphorus magnetic resonance spectroscopy study. *Circulation*, 2009; 119: 1918–1924.
108. Weiss RG, Gerstenblith G, Bottomley PA. ATP flux through creatine kinase in the normal, stressed, and failing human heart. *Proc. Natl. Acad. Sci. U. S. A.*, 2005; 102: 808–813.
109. Nagarajan V, Gopalan V, Kaneko M, Angeli V, Gluckman P, Richards AM, Kuchel PW, Velan SS. Cardiac function and lipid distribution in rats fed a high-fat diet: in vivo magnetic resonance imaging and spectroscopy. *Am. J. Physiol. Heart Circ. Physiol.* 2013; 304: H1495–H1504.
110. Toyo-oka T, Nagayama K, Suzuki J, Sugimoto T. Noninvasive assessment of cardiomyopathy development with simultaneous measurement of topical <sup>1</sup>H- and <sup>31</sup>P-magnetic resonance spectroscopy. *Circulation*, 1992; 86: 295–301.
111. Hankiewicz JH, Banke NH, Farjah M, Lewandowski ED. Early impairment of transmural principal strains in the left ventricular wall after short-term, high-fat feeding of mice predisposed to cardiac steatosis. *Circ. Cardiovasc. Imaging*, 2010; 3: 710–717.
112. Phillips D, Ten Hove M, Schneider JE, Wu CO, Sebag-Montefiore L, Aponte AM, Lygate CA, Wallis J, Clarke K, Watkins H, Balaban RS, Neubauer S. Mice over-expressing the myocardial creatine transporter develop progressive heart failure and show decreased glycolytic capacity. *J. Mol. Cell. Cardiol.* 2010; 48: 582–590.
113. Lygate CA, Bohl S, ten Hove M, Faller KM, Ostrowski PJ, Zervou S, Medway DJ, Aksentijevic D, Sebag-Montefiore L, Wallis J, Clarke K, Watkins H, Schneider JE, Neubauer S. Moderate elevation of intracellular creatine by targeting the creatine transporter protects mice from acute myocardial infarction. *Cardiovasc. Res.* 2012; 96: 466–475.
114. Bollano E, Omerovic E, Svensson H, Waagstein F, Fu M. Cardiac remodeling rather than disturbed myocardial energy metabolism is associated with cardiac dysfunction in diabetic rats. *Int. J. Cardiol.* 2007; 114: 195–201.
115. Abdurrahim D, Ciapaite J, Wessels B, Nabben M, Luiken JJ, Nicolay K, Prompers JJ. Cardiac diastolic dysfunction in high-fat diet fed mice is associated with lipotoxicity without impairment of cardiac energetics in vivo. *Biochim. Biophys. Acta*, 2014; 1842: 1525–1537.
116. Gupta A, Chacko VP, Weiss RG. Abnormal energetics and ATP depletion in pressure-overload mouse hearts: in vivo high-energy phosphate concentration measures by noninvasive magnetic resonance. *Am. J. Physiol. Heart Circ. Physiol.* 2009; 297: H59–H64.
117. Naumova AV, Chacko VP, Ouwerkerk R, Stull L, Marban E, Weiss RG. Xanthine oxidase inhibitors improve energetics and function after infarction in failing mouse hearts. *Am. J. Physiol. Heart Circ. Physiol.* 2006; 290: H837–H843.
118. Omerovic E, Bollano E, Mobini R, Madhu B, Kujacic V, Soussi B, Hjalmarson A, Waagstein F. Selective beta(1)-blockade improves cardiac bioenergetics and function and decreases neuroendocrine activation in rats during early postinfarct remodeling. *Biochem. Biophys. Res. Commun.* 2001; 281: 491–498.
119. Bottomley PA, Weiss RG. Noninvasive localized MR quantification of creatine kinase metabolites in normal and infarcted canine myocardium. *Radiology*, 2001; 219: 411–418.
120. Xiong Q, Ye L, Zhang P, Lepley M, Swingen C, Zhang L, Kaufman DS, Zhang J. Bioenergetic and functional consequences of cellular therapy: activation of endogenous cardiovascular progenitor cells. *Circ. Res.* 2012; 111: 455–468.
121. Miller DD, Salinas F, Walsh RA. Simultaneous cardiac mechanics and phosphorus-31 NMR spectroscopy during global myocardial ischemia and reperfusion in the intact dog. *Magn. Reson. Med.* 1991; 17: 41–52.
122. Omerovic E, Bollano E, Mobini R, Kujacic V, Madhu B, Soussi B, Fu M, Hjalmarson A, Waagstein F, Isgaard J. Growth hormone improves bioenergetics and decreases catecholamines in postinfarct rat hearts. *Endocrinology*, 2000; 141: 4592–4599.
123. Lorentzon M, Ramunddal T, Bollano E, Soussi B, Waagstein F, Omerovic E. In vivo effects of myocardial creatine depletion on left ventricular function, morphology, and energy metabolism—consequences in acute myocardial infarction. *J. Card. Fail.* 2007; 13: 230–237.
124. Bakermans AJ, Dodd MS, Nicolay K, Prompers JJ, Tyler DJ, Houten SM. Myocardial energy shortage and unmet anaplerotic needs in the fasted long-chain acyl-CoA dehydrogenase knockout mouse. *Cardiovasc. Res.* 2013; 100: 441–449.
125. Maslov MY, Chacko VP, Stuber M, Moens AL, Kass DA, Champion HC, Weiss RG. Altered high-energy phosphate metabolism predicts contractile dysfunction and subsequent ventricular remodeling in pressure-overload hypertrophy mice. *Am. J. Physiol. Heart Circ. Physiol.* 2007; 292: H387–H391.
126. Gupta A, Chacko VP, Schar M, Akki A, Weiss RG. Impaired ATP kinetics in failing in vivo mouse heart. *Circ. Cardiovasc. Imaging*, 2011; 4: 42–50.
127. Gupta A, Rohlfen C, Leppo MK, Chacko VP, Wang Y, Steenbergen C, Weiss RG. Creatine kinase-overexpression improves myocardial energetics, contractile dysfunction and survival in murine doxorubicin cardiotoxicity. *PLoS One*, 2013; 8: e74675.
128. Schroeder MA, Cochlin LE, Heather LC, Clarke K, Radda GK, Tyler DJ. In vivo assessment of pyruvate dehydrogenase flux in the heart using hyperpolarized carbon-13 magnetic resonance. *Proc. Natl. Acad. Sci. U S A*, 2008; 105: 12 051–12 056.
129. Atherton HJ, Dodd MS, Heather LC, Schroeder MA, Griffin JL, Radda GK, Clarke K, Tyler DJ. Role of pyruvate dehydrogenase inhibition in the development of hypertrophy in the hyperthyroid rat heart: a combined magnetic resonance imaging and hyperpolarized magnetic resonance spectroscopy study. *Circulation*, 2011; 123: 2552–2561.
130. Schroeder MA, Lau AZ, Chen AP, Gu Y, Nagendran J, Barry J, Hu X, Dyck JR, Tyler DJ, Clarke K, Connelly KA, Wright GA, Cunningham CH. Hyperpolarized <sup>13</sup>C magnetic resonance reveals early- and late-onset changes to in vivo pyruvate metabolism in the failing heart. *Eur. J. Heart Fail.* 2013; 15: 130–140.
131. Dodd MS, Ball DR, Schroeder MA, Le Page LM, Atherton HJ, Heather LC, Seymour AM, Ashrafian H, Watkins H, Clarke K, Tyler DJ. In vivo alterations in cardiac metabolism and function in the spontaneously hypertensive rat heart. *Cardiovasc. Res.* 2012; 95: 69–76.
132. Dodd MS, Atherton HJ, Carr CA, Stuckey DJ, West JA, Griffin JL, Radda GK, Clarke K, Heather LC, Tyler DJ. Impaired in vivo mitochondrial Krebs cycle activity after myocardial infarction assessed using hyperpolarized magnetic resonance spectroscopy. *Circ. Cardiovasc. Imaging*, 2014; 7: 895–904.

133. El-Sharkawy AM, Gabr RE, Schar M, Weiss RG, Bottomley PA. Quantification of human high-energy phosphate metabolite concentrations at 3 T with partial volume and sensitivity corrections. *NMR Biomed.* 2013; 26: 1363–1371.
134. Swain JL, Sabina RL, Peyton RB, Jones RN, Wechsler AS, Holmes EW. Derangements in myocardial purine and pyrimidine nucleotide metabolism in patients with coronary artery disease and left ventricular hypertrophy. *Proc. Natl. Acad. Sci. U. S. A.*, 1982; 79: 655–659.
135. Ordidge RJ, Connelly A, Lohman JAB. Image-selected in vivo spectroscopy (ISIS). A new technique for spatially selective NMR spectroscopy. *J. Magn. Reson.* 1986; 66: 283–294.
136. Lamb HJ, Doornbos J, den Hollander JA, Luyten PR, Beyerbach HP, van der Wall EE, de Roos A. Reproducibility of human cardiac  $^{31}\text{P}$ -NMR spectroscopy. *NMR Biomed.* 1996; 9: 217–227.
137. Von Kienlin M, Mejia R. Spectral localization with optimal pointspread function. *J. Magn. Reson.* 1991; 94: 268–287.
138. Löffler R, Sauter R, Kolem H, Haase M, von Kienlin M. Localized spectroscopy from anatomically matched compartments: improved sensitivity and localization for cardiac  $^{31}\text{P}$  MRS in humans. *J. Magn. Reson.* 1998; 134: 287–299.
139. Omerovic E, Basetti M, Bollano E, Bohloly YM, Tornell J, Isgaard J, Hjalmarson A, Soussi B, Waagstein F. In vivo metabolic imaging of cardiac bioenergetics in transgenic mice. *Biochem. Biophys. Res. Commun.* 2000; 271: 222–228.
140. Chacko VP, Aresta F, Chacko SM, Weiss RG. MRI/MRS assessment of in vivo murine cardiac metabolism, morphology, and function at physiological heart rates. *Am. J. Physiol. Heart Circ. Physiol.* 2000; 279: H2218–H2224.
141. Fogel U, Jacoby C, Godecke A, Schrader J. In vivo 2D mapping of impaired murine cardiac energetics in NO-induced heart failure. *Magn. Reson. Med.* 2007; 57: 50–58.
142. Schaefer S, Gober JR, Schwartz GG, Twieg DB, Weiner MW, Massie B. In vivo phosphorus-31 spectroscopic imaging in patients with global myocardial disease. *Am. J. Cardiol.* 1990; 65: 1154–1161.
143. Rijzewijk LJ, Jonker JT, van der Meer RW, Lubberink M, de Jong HW, Romijn JA, Bax JJ, de Roos A, Heine RJ, Twisk JW, Windhorst AD, Lammertsma AA, Smit JW, Diamant M, Lamb HJ. Effects of hepatic triglyceride content on myocardial metabolism in type 2 diabetes. *J. Am. Coll. Cardiol.* 2010; 56: 225–233.
144. Fragasso G, De Cobelli F, Spoladore R, Esposito A, Salerno A, Calori G, Montanaro C, Maranta F, Lattuada G, Margonato A, Del Maschio A, Perseghin G. Resting cardiac energy metabolism is inversely associated with heart rate in healthy young adult men. *Am. Heart J.* 2011; 162: 136–141.
145. Klug G, Zwick RH, Frick M, Wolf C, Schocke MF, Conci E, Jaschke W, Pachinger O, Metzler B. Impact of exercise capacity on myocardial high-energy phosphate metabolism. *Int. J. Sports Med.* 2007; 28: 667–672.
146. Kuno S, Ogawa T, Katsuta S, Itai Y. In vivo human myocardial metabolism during aerobic exercise by phosphorus-31 nuclear magnetic resonance spectroscopy. *Eur. J. Appl. Physiol. Occup. Physiol.* 1994; 69: 488–491.
147. Hudsmith LE, Tyler DJ, Emmanuel Y, Petersen SE, Francis JM, Watkins H, Clarke K, Robson MD, Neubauer S.  $(^{31}\text{P})$  cardiac magnetic resonance spectroscopy during leg exercise at 3 Tesla. *Int. J. Cardiovasc. Imaging.* 2009; 25: 819–826.
148. Lamb HJ, Beyerbach HP, Ouwerkerk R, Doornbos J, Pluim BM, van der Wall EE, van der Laarse A, de Roos A. Metabolic response of normal human myocardium to high-dose atropine-dobutamine stress studied by  $^{31}\text{P}$ -MRS. *Circulation.* 1997; 96: 2969–2977.
149. Schaefer S, Schwartz GG, Steinman SK, Meyerhoff DJ, Massie BM, Weiner MW. Metabolic response of the human heart to inotropic stimulation: in vivo phosphorus-31 studies of normal and cardiomyopathic myocardium. *Magn. Reson. Med.* 1992; 25: 260–272.
150. Swindle MM, Makin A, Herron AJ, Clubb FJ Jr, Frazier KS. Swine as models in biomedical research and toxicology testing. *Vet. Pathol.* 2012; 49: 344–356.
151. Zaragoza C, Gomez-Guerrero C, Martin-Ventura JL, Blanco-Colio L, Lavin B, Mallavia B, Tarin C, Mas S, Ortiz A, Egidio J. Animal models of cardiovascular diseases. *J. Biomed. Biotechnol.* 2011; 2011: 1–13.
152. Camacho SA, Lanzer P, Toy BJ, Gober J, Valenza M, Botvinick EH, Weiner MW. In vivo alterations of high-energy phosphates and intracellular pH during reversible ischemia in pigs: a  $^{31}\text{P}$  magnetic resonance spectroscopy study. *Am. Heart J.* 1988; 116: 701–708.
153. Schwartz GG, Steinman S, Garcia J, Greyson C, Massie B, Weiner MW. Energetics of acute pressure overload of the porcine right ventricle. In vivo  $^{31}\text{P}$  nuclear magnetic resonance. *J. Clin. Invest.* 1992; 89: 909–918.
154. Rath DP, Bailey M, Zhang H, Jiang Z, Abduljalil AM, Weisbrode S, Hamlin RL, Robitaille PM.  $^{31}\text{P}$ -nuclear magnetic resonance studies of chronic myocardial ischemia in the Yucatan micropig. *J. Clin. Invest.* 1995; 95: 151–157.
155. Zhang J, Murakami Y, Zhang Y, Cho YK, Ye Y, Gong G, Bache RJ, Ugurbil K, From AH. Oxygen delivery does not limit cardiac performance during high work states. *Am. J. Physiol.* 1999; 277: H50–H57.
156. Wu F, Zhang EY, Zhang J, Bache RJ, Beard DA. Phosphate metabolite concentrations and ATP hydrolysis potential in normal and ischaemic hearts. *J. Physiol.* 2008; 586: 4193–4208.
157. Dell'Italia LJ, Evanochko WT, Blackwell GG, Pearce DJ, Pohost GM. Relationship between shortening load, contractility, and myocardial energetics in intact dog. *Am. J. Physiol.* 1993; 264: H2180–H2187.
158. Cho YK, Merkle H, Zhang J, Tsekos NV, Bache RJ, Ugurbil K. Noninvasive measurements of transmural myocardial metabolites using 3-D  $(^{31}\text{P})$  NMR spectroscopy. *Am. J. Physiol. Heart Circ. Physiol.* 2001; 280: H489–H497.
159. Robitaille PM, Merkle H, Lew B, Path G, Hendrich K, Lindstrom P, From AH, Garwood M, Bache RJ, Ugurbil K. Transmural high energy phosphate distribution and response to alterations in workload in the normal canine myocardium as studied with spatially localized  $^{31}\text{P}$  NMR spectroscopy. *Magn. Reson. Med.* 1990; 16: 91–116.
160. Naumova AV, Weiss RG, Chacko VP. Regulation of murine myocardial energy metabolism during adrenergic stress studied by in vivo  $^{31}\text{P}$  NMR spectroscopy. *Am. J. Physiol. Heart Circ. Physiol.* 2003; 285: H1976–H1979.
161. Dawson J, Walters M. Uric acid and xanthine oxidase: future therapeutic targets in the prevention of cardiovascular disease? *Br. J. Clin. Pharmacol.* 2006; 62: 633–644.
162. Omerovic E, Bollano E, Soussi B, Waagstein F. Selective beta1-blockade attenuates post-infarct remodelling without improvement in myocardial energy metabolism and function in rats with heart failure. *Eur. J. Heart Fail.* 2003; 5: 725–732.
163. Bohloly YM, Bollano E, Mobini R, Soussi B, Tornell J, Omerovic E. Selective cerebral overexpression of growth hormone alters cardiac function, morphology, energy metabolism and catecholamines in transgenic mice. *Growth Horm. IGF Res.* 2005; 15: 148–155.
164. Wolfe CL, Donnelly TJ, Sievers R, Parmley WW. Myocardial protection with verapamil during ischaemia and reperfusion: dissociation between myocardial salvage and the degree of ATP depletion during ischaemia. *Cardiovasc. Res.* 1991; 25: 101–109.
165. Bittl JA, Ingwall JS. Reaction rates of creatine kinase and ATP synthesis in the isolated rat heart. A  $^{31}\text{P}$  NMR magnetization transfer study. *J. Biol. Chem.* 1985; 260: 3512–3517.
166. De Graaf RA. *In vivo NMR Spectroscopy: Principles and Techniques* 2nd edn. Wiley: Chichester, 2007.
167. Robitaille PM, Abduljalil A, Rath D, Zhang H, Hamlin RL. Transmural saturation transfer analysis of the creatine kinase system in the mammalian heart. *Magn. Reson. Med.* 1993; 30: 4–10.
168. Bottomley PA, Hardy CJ. Mapping creatine kinase reaction rates in human brain and heart with 4 Tesla saturation transfer  $^{31}\text{P}$  NMR. *J. Magn. Reson.* 1992; 99: 443–448.
169. Ouwerkerk R, Bottomley PA. On neglecting chemical exchange effects when correcting in vivo  $(^{31}\text{P})$  MRS data for partial saturation. *J. Magn. Reson.* 2001; 148: 425–435.
170. Spencer RG, Fishbein KW, Galban CJ. Pitfalls in the measurement of metabolite concentrations using the one-pulse experiment in in vivo NMR: commentary on 'On neglecting chemical exchange effects when correcting in vivo  $(^{31}\text{P})$  MRS data for partial saturation'. *J. Magn. Reson.* 2001; 149: 251–257.
171. Ouwerkerk R, Bottomley PA. On neglecting chemical exchange when correcting in vivo  $(^{31}\text{P})$  MRS data for partial saturation: commentary on: 'Pitfalls in the measurement of metabolite concentrations using the one-pulse experiment in in vivo NMR'. *J. Magn. Reson.* 2001; 149: 282–286.
172. Osbakken M, Douglas PS, Ivanics T, Zhang DN, Van Winkle T. Creatinine kinase kinetics studied by phosphorus-31 nuclear magnetic resonance in a canine model of chronic hypertension-induced cardiac hypertrophy. *J. Am. Coll. Cardiol.* 1992; 19: 223–228.
173. Murakami Y, Zhang J, Eijgelshoven MH, Chen W, Carlyle WC, Zhang Y, Gong G, Bache RJ. Myocardial creatine kinase kinetics in hearts



- with postinfarction left ventricular remodeling. *Am. J. Physiol.* 1999; 276: H892–H900.
174. Hsieh PS, Balaban RS.  $^{31}\text{P}$  imaging of in vivo creatine kinase reaction rates. *J. Magn. Reson.* 1987; 74: 574–579.
  175. Bottomley PA, Ouwervkerk R. The dual-angle method for fast, sensitive T1 measurement in vivo with low-angle adiabatic pulses. *J. Magn. Reson. Ser. B*, 1994; 104: 159–167.
  176. Bottomley PA, Ouwervkerk R, Lee RF, Weiss RG. Four-angle saturation transfer (FAST) method for measuring creatine kinase reaction rates in vivo. *Magn. Reson. Med.* 2002; 47: 850–863.
  177. Tyler DJ, Lopez O, Cole MA, Carr CA, Stuckey DJ, Lakatta E, Clarke K, Spencer RG. Ongoing dual-angle measurements for the correction of partial saturation in  $^{31}\text{P}$  MR spectroscopy. *Magn. Reson. Med.* 2010; 64: 957–966.
  178. Xiong Q, Li Q, Mansoor A, Jameel MN, Du F, Chen W, Zhang J. Novel strategy for measuring creatine kinase reaction rate in the in vivo heart. *Am. J. Physiol. Heart Circ. Physiol.* 2009; 297: H1010–H1019.
  179. Xiong Q, Du F, Zhu X, Zhang P, Suntharalingam P, Ippolito J, Kamdar FD, Chen W, Zhang J. ATP production rate via creatine kinase or ATP synthase in vivo: a novel superfast magnetization saturation transfer method. *Circ. Res.* 2011; 108: 653–663.
  180. Bashir A, Gropler R. Reproducibility of creatine kinase reaction kinetics in human heart: a P time-dependent saturation transfer spectroscopy study. *NMR Biomed.* 2014; 27: 663–671.
  181. Brindle KM, Rajagopalan B, Williams DS, Detre JA, Simplaceanu E, Ho C, Radda GK.  $^{31}\text{P}$  NMR measurements of myocardial pH in vivo. *Biochem. Biophys. Res. Commun.* 1988; 151: 70–77.
  182. Blamire AM, Rajagopalan B, Radda GK. Measurement of myocardial pH by saturation transfer in man. *Magn. Reson. Med.* 1999; 41: 198–203.
  183. Walecki J, Michalak MJ, Michalak E, Bilinska ZT, Ruzyllo W. Usefulness of  $^1\text{H}$  MR spectroscopy in the evaluation of myocardial metabolism in patients with dilated idiopathic cardiomyopathy: pilot study. *Acad. Radiol.* 2003; 10: 1187–1192.
  184. Ugurbil K, Pettein M, Maidan R, Michurski S, Cohn JN, From AH. High resolution proton NMR studies of perfused rat hearts. *FEBS Lett.* 1984; 167: 73–78.
  185. Griffin JL, Williams HJ, Sang E, Nicholson JK. Abnormal lipid profile of dystrophic cardiac tissue as demonstrated by one- and two-dimensional magic-angle spinning ( $^1\text{H}$ ) NMR spectroscopy. *Magn. Reson. Med.* 2001; 46: 249–255.
  186. Chapman D, Morrison A. Physical studies of phospholipids. IV. High resolution nuclear magnetic resonance spectra of phospholipids and related substances. *J. Biol. Chem.* 1966; 241: 5044–5052.
  187. Wu J, Yang L, Yang J, Yang CH, Zhang XH. Gender-specific normal levels of myocardial metabolites determined by localized  $^1\text{H}$ -magnetic resonance spectroscopy. *J. Int. Med. Res.* 2012; 40: 1507–1512.
  188. Ith M, Stettler C, Xu J, Boesch C, Kreis R. Cardiac lipid levels show diurnal changes and long-term variations in healthy human subjects. *NMR Biomed.* 2014; 27: 1285–1292.
  189. Frahm J, Merboldt KD, Hancic W. Localized proton spectroscopy using stimulated echoes. *J. Magn. Reson.* 1987; 72: 502.
  190. Bottomley PA. Spatial localization in NMR spectroscopy in vivo. *Ann. N. Y. Acad. Sci.* 1987; 508: 333–348.
  191. de Graaf RA, Rothman DL. In vivo detection and quantification of scalar coupled H-1 NMR resonances. *Concept Magn. Res.* 2001; 13: 32–76.
  192. Pattany PM, Massand MG, Bowen BC, Quencer RM. Quantitative analysis of the effects of physiologic brain motion on point-resolved spectroscopy. *Am. J. Neuroradiol.* 2006; 27: 1070–1073.
  193. Weiss K, Summermatter S, Stoek CT, Kozerke S. Compensation of signal loss due to cardiac motion in point-resolved spectroscopy of the heart. *Magn. Reson. Med.* 2013; 72: 1201–1207.
  194. Haase A, Frahm J, Hancic W, Matthaei D.  $^1\text{H}$  NMR chemical shift selective (CHESS) imaging. *Phys. Med. Biol.* 1985; 30: 341–344.
  195. Schneider J, Fekete E, Weisser A, Neubauer S, von Kienlin M. Reduced ( $^1\text{H}$ -NMR) visibility of creatine in isolated rat hearts. *Magn. Reson. Med.* 2000; 43: 497–502.
  196. Weiss K, Martini N, Boesiger P, Kozerke S. Metabolic MR imaging of regional triglyceride and creatine content in the human heart. *Magn. Reson. Med.* 2012; 68: 1696–1704.
  197. Liu CY, Liu YC, Venkatesh BA, Lima JA, Bluemke DA, Steenbergen C. Heterogeneous distribution of myocardial steatosis—an ex vivo evaluation. *Magn. Reson. Med.* 2012; 68: 1–7.
  198. Mahmod M, Bull S, Suttie JJ, Pal N, Holloway C, Dass S, Myerson SG, Schneider JE, De Silva R, Petrou M, Sayeed R, Westaby S, Clelland C, Francis JM, Ashrafian H, Karamitsos TD, Neubauer S. Myocardial steatosis and left ventricular contractile dysfunction in patients with severe aortic stenosis. *Circ. Cardiovasc. Imaging*, 2013; 6: 808–816.
  199. O'Connor RD, Xu J, Ewald GA, Ackerman JJ, Peterson LR, Gropler RJ, Bashir A. Intramyocardial triglyceride quantification by magnetic resonance spectroscopy: in vivo and ex vivo correlation in human subjects. *Magn. Reson. Med.* 2011; 65: 1234–1238.
  200. Kreis R, Felblinger J, Jung B, Boesch C. In vivo  $^1\text{H}$ -MR spectroscopy of the human heart. *MAGMA*, 1998; 6: 164–167.
  201. Bottomley PA, Weiss RG. Non-invasive magnetic-resonance detection of creatine depletion in non-viable infarcted myocardium. *Lancet*, 1998; 351: 714–718.
  202. Reingold JS, McGavock JM, Kaka S, Tillery T, Victor RG, Szczepaniak LS. Determination of triglyceride in the human myocardium by magnetic resonance spectroscopy: reproducibility and sensitivity of the method. *Am. J. Physiol. Endocrinol. Metab.* 2005; 289: E935–E939.
  203. van der Meer RW, Hammer S, Smit JW, Frolich M, Bax JJ, Diamant M, Rijzewijk LJ, de Roos A, Romijn JA, Lamb HJ. Short-term caloric restriction induces accumulation of myocardial triglycerides and decreases left ventricular diastolic function in healthy subjects. *Diabetes*, 2007; 56: 2849–2853.
  204. Schrauwen-Hinderling VB, Hesselink MK, Meex R, van der Made S, Schar M, Lamb H, Wildberger JE, Glatz J, Snoep G, Kooi ME, Schrauwen P. Improved ejection fraction after exercise training in obesity is accompanied by reduced cardiac lipid content. *J. Clin. Endocrinol. Metab.* 2010; 95: 1932–1938.
  205. Hammer S, Snel M, Lamb HJ, Jazet IM, van der Meer RW, Pijl H, Meinders EA, Romijn JA, de Roos A, Smit JW. Prolonged caloric restriction in obese patients with type 2 diabetes mellitus decreases myocardial triglyceride content and improves myocardial function. *J. Am. Coll. Cardiol.* 2008; 52: 1006–1012.
  206. Scherer T, Wolf P, Winhofer Y, Duan H, Einwallner E, Gessl A, Luger A, Trattinig S, Hoffmann M, Niessner A, Baumgartner-Parzer S, Krssak M, Krebs M. Levothyroxine replacement in hypothyroid humans reduces myocardial lipid load and improves cardiac function. *J. Clin. Endocrinol. Metab.* 2014; 99: E2341–E2346.
  207. Schrauwen-Hinderling VB, Meex RC, Hesselink MK, van de Weijer T, Leiner T, Schar M, Lamb HJ, Wildberger JE, Glatz JF, Schrauwen P, Kooi ME. Cardiac lipid content is unresponsive to a physical activity training intervention in type 2 diabetic patients, despite improved ejection fraction. *Cardiovasc. Diabetol.* 2011; 10: 47.
  208. Bakermans AJ, van Weeghel M, Denis S, Nicolay K, Prompers JJ, Houten SM. Carnitine supplementation attenuates myocardial lipid accumulation in long-chain acyl-CoA dehydrogenase knockout mice. *J. Inher. Metab. Dis.* 2013; 36: 973–981.
  209. Faller KM, Medway DJ, Aksentijevic D, Sebag-Montefiore L, Schneider JE, Lygate CA, Neubauer S. Ribose supplementation alone or with elevated creatine does not preserve high energy nucleotides or cardiac function in the failing mouse heart. *PLoS One*, 2013; 8: e66461.
  210. Liu CY, Redheuil A, Ouwervkerk R, Lima JA, Bluemke DA. Myocardial fat quantification in humans: evaluation by two-point water–fat imaging and localized proton spectroscopy. *Magn. Reson. Med.* 2010; 63: 892–901.
  211. Saranathan M, Glockner J. Three-dimensional Dixon fat–water separated rapid breathheld imaging of myocardial infarction. *J. Magn. Reson. Imaging*, 2013; 38: 1362–1368.
  212. Dixon WT. Simple proton spectroscopic imaging. *Radiology*, 1984; 153: 189–194.
  213. Glover GH, Schneider E. Three-point Dixon technique for true water/fat decomposition with B0 inhomogeneity correction. *Magn. Reson. Med.* 1991; 18: 371–383.
  214. Berglund J, Ahlstrom H, Johansson L, Kullberg J. Two-point Dixon method with flexible echo times. *Magn. Reson. Med.* 2011; 65: 994–1004.
  215. Eggers H, Brendel B, Duijndam A, Herigault G. Dual-echo Dixon imaging with flexible choice of echo times. *Magn. Reson. Med.* 2011; 65: 96–107.
  216. Reeder SB, Pineda AR, Wen Z, Shimakawa A, Yu H, Brittain JH, Gold GE, Beaulieu CH, Pelc NJ. Iterative decomposition of water and fat with echo asymmetry and least-squares estimation (IDEAL): application with fast spin-echo imaging. *Magn. Reson. Med.* 2005; 54: 636–644.



217. Hernando D, Haldar JP, Sutton BP, Ma J, Kellman P, Liang ZP. Joint estimation of water/fat images and field inhomogeneity map. *Magn. Reson. Med.* 2008; 59: 571–580.
218. Ma J. Dixon techniques for water and fat imaging. *J. Magn. Reson. Imaging*, 2008; 28: 543–558.
219. Goldfarb JW. Fat–water separated delayed hyperenhanced myocardial infarct imaging. *Magn. Reson. Med.* 2008; 60: 503–509.
220. Tyler DJ. Cardiovascular applications of hyperpolarized MRI. *Curr. Cardiovasc. Imaging Rep.* 2011; 4: 108–115.
221. Ardenkjaer-Larsen JH, Fridlund B, Gram A, Hansson G, Hansson L, Lerche MH, Servin R, Thaning M, Golman K. Increase in signal-to-noise ratio of > 10,000 times in liquid-state NMR. *Proc. Natl. Acad. Sci. U S A*, 2003; 100: 10 158–10 163.
222. Gallagher FA, Kettunen MI, Brindle KM. Biomedical applications of hyperpolarized  $^{13}\text{C}$  magnetic resonance imaging. *Prog. Nucl. Magn. Reson. Spectrosc.* 2009; 55: 285–295.
223. Schroeder MA, Atherton HJ, Cochlin LE, Clarke K, Radda GK, Tyler DJ. The effect of hyperpolarized tracer concentration on myocardial uptake and metabolism. *Magn. Reson. Med.* 2009; 61: 1007–1014.
224. Mansson S, Johansson E, Magnusson P, Chai CM, Hansson G, Petersson JS, Stahlberg F, Golman K.  $^{13}\text{C}$  imaging—a new diagnostic platform. *Eur. Radiol.* 2006; 16: 57–67.
225. Rider OJ, Tyler DJ. Clinical implications of cardiac hyperpolarized magnetic resonance imaging. *J. Cardiovasc. Magn. Reson.* 2013; 15: 93.
226. Tyler DJ, Schroeder MA, Cochlin LE, Clarke K, Radda GK. Application of hyperpolarized magnetic resonance in the study of cardiac metabolism. *Appl. Magn. Reson.* 2008; 34: 523–531.
227. Dodd MS, Ball V, Bray R, Ashrafian H, Watkins H, Clarke K, Tyler DJ. In vivo mouse cardiac hyperpolarized magnetic resonance spectroscopy. *J. Cardiovasc. Magn. Reson.* 2013; 15: 19.
228. Golman K, Petersson JS, Magnusson P, Johansson E, Akeson P, Chai CM, Hansson G, Mansson S. Cardiac metabolism measured noninvasively by hyperpolarized  $^{13}\text{C}$  MRI. *Magn. Reson. Med.* 2008; 59: 1005–1013.
229. Lau AZ, Chen AP, Ghugre NR, Ramanan V, Lam WW, Connelly KA, Wright GA, Cunningham CH. Rapid multislice imaging of hyperpolarized  $^{13}\text{C}$  pyruvate and bicarbonate in the heart. *Magn. Reson. Med.* 2010; 64: 1323–1331.
230. Lau AZ, Chen AP, Cunningham CH. Integrated Bloch–Siebert B(1) mapping and multislice imaging of hyperpolarized (1)(3) $\text{C}$  pyruvate and bicarbonate in the heart. *Magn. Reson. Med.* 2012; 67: 62–71.
231. Merritt ME, Harrison C, Storey C, Jeffrey FM, Sherry AD, Malloy CR. Hyperpolarized  $^{13}\text{C}$  allows a direct measure of flux through a single enzyme-catalyzed step by NMR. *Proc. Natl. Acad. Sci. U S A*, 2007; 104: 19 773–19 777.
232. Atherton HJ, Schroeder MA, Dodd MS, Heather LC, Carter EE, Cochlin LE, Nagel S, Sibson NR, Radda GK, Clarke K, Tyler DJ. Validation of the in vivo assessment of pyruvate dehydrogenase activity using hyperpolarized  $^{13}\text{C}$  MRS. *NMR Biomed.* 2011; 24: 201–208.
233. Lauritzen MH, Laustsen C, Butt SA, Magnusson P, Sogaard LV, Ardenkjaer-Larsen JH, Akeson P. Enhancing the  $^{13}\text{C}$  bicarbonate signal in cardiac hyperpolarized  $^{13}\text{C}$  pyruvate MRS studies by infusion of glucose, insulin and potassium. *NMR Biomed.* 2013; 26: 1496–1500.
234. Schroeder MA, Atherton HJ, Heather LC, Griffin JL, Clarke K, Radda GK, Tyler DJ. Determining the in vivo regulation of cardiac pyruvate dehydrogenase based on label flux from hyperpolarized  $^{13}\text{C}$  pyruvate. *NMR Biomed.* 2011; 24: 980–987.
235. Menichetti L, Frijia F, Flori A, Wiesinger F, Lionetti V, Giovannetti G, Aquaro GD, Recchia FA, Ardenkjaer-Larsen JH, Santarelli MF, Lombardi M. Assessment of real-time myocardial uptake and enzymatic conversion of hyperpolarized  $^{13}\text{C}$  pyruvate in pigs using slice selective magnetic resonance spectroscopy. *Contrast Media Mol. Imaging*, 2012; 7: 85–94.
236. Schroeder MA, Swietach P, Atherton HJ, Gallagher FA, Lee P, Radda GK, Clarke K, Tyler DJ. Measuring intracellular pH in the heart using hyperpolarized carbon dioxide and bicarbonate: a  $^{13}\text{C}$  and  $^{31}\text{P}$  magnetic resonance spectroscopy study. *Cardiovasc. Res.* 2010; 86: 82–91.
237. Schroeder MA, Atherton HJ, Dodd MS, Lee P, Cochlin LE, Radda GK, Clarke K, Tyler DJ. The cycling of acetyl-coenzyme A through acetylcarnitine buffers cardiac substrate supply: a hyperpolarized  $^{13}\text{C}$  magnetic resonance study. *Circ. Cardiovasc. Imaging*, 2012; 5: 201–209.
238. Schroeder MA, Atherton HJ, Ball DR, Cole MA, Heather LC, Griffin JL, Clarke K, Radda GK, Tyler DJ. Real-time assessment of Krebs cycle metabolism using hyperpolarized  $^{13}\text{C}$  magnetic resonance spectroscopy. *Faseb J.* 2009; 23: 2529–2538.
239. Chen AP, Hurd RE, Schroeder MA, Lau AZ, Gu YP, Lam WW, Barry J, Tropp J, Cunningham CH. Simultaneous investigation of cardiac pyruvate dehydrogenase flux, Krebs cycle metabolism and pH, using hyperpolarized  $^{13}\text{C}$  pyruvate in vivo. *NMR Biomed.* 2012; 25: 305–311.
240. Josan S, Park JM, Hurd R, Yen YF, Pfefferbaum A, Spielman D, Mayer D. In vivo investigation of cardiac metabolism in the rat using MRS of hyperpolarized  $^{13}\text{C}$  and  $^{15}\text{N}$  pyruvate. *NMR Biomed.* 2013; 26: 1680–1687.
241. Chen AP, Kurhanewicz J, Bok R, Xu D, Joun D, Zhang V, Nelson SJ, Hurd RE, Vigneron DB. Feasibility of using hyperpolarized  $^{13}\text{C}$  lactate as a substrate for in vivo metabolic  $^{13}\text{C}$  MRS studies. *Magn. Reson. Imaging*, 2008; 26: 721–726.
242. Mayer D, Yen YF, Josan S, Park JM, Pfefferbaum A, Hurd RE, Spielman DM. Application of hyperpolarized  $^{13}\text{C}$  lactate for the in vivo investigation of cardiac metabolism. *NMR Biomed.* 2012; 25: 1119–1124.
243. Moreno KX, Sabelhaus SM, Merritt ME, Sherry AD, Malloy CR. Competition of pyruvate with physiological substrates for oxidation by the heart: implications for studies with hyperpolarized  $^{13}\text{C}$  pyruvate. *Am. J. Physiol. Heart Circ. Physiol.* 2010; 298: H1556–H1564.
244. Chen AP, Lau JY, Alvares RD, Cunningham CH. Using  $^{13}\text{C}$  lactic acid for hyperpolarized  $^{13}\text{C}$  MR cardiac studies. *Magn. Reson. Med.* 2014.
245. Ball DR, Rowlands B, Dodd MS, Le Page L, Ball V, Carr CA, Clarke K, Tyler DJ. Hyperpolarized butyrate: a metabolic probe of short chain fatty acid metabolism in the heart. *Magn. Reson. Med.* 2013; 71: 1663–1669.
246. Nelson SJ, Kurhanewicz J, Vigneron DB, Larson PE, Harzstark AL, Ferrone M, van Crielinge M, Chang JW, Bok R, Park I, Reed G, Carvajal L, Small EJ, Munster P, Weinberg VK, Ardenkjaer-Larsen JH, Chen AP, Hurd RE, Odegardstuen LI, Robb FJ, Tropp J, Murray JA. Metabolic imaging of patients with prostate cancer using hyperpolarized  $^{13}\text{C}$  pyruvate. *Sci. Transl. Med.* 2013; 5: 198ra108.